

Your Interlibrary Loan request has been sent by email in a PDF format.

If this PDF arrives with an incorrect OCLC status, please contact lending located below.

Concerning Copyright Restrictions

The copyright law of the United States (Title 17, United States Code) governs the making of photocopies or other reproductions of copyrighted materials. Under certain conditions specified in the law, libraries and archives are authorized to furnish a photocopy or other reproduction. One of these specified conditions is that the photocopy or reproduction is not to be "used for any purpose other than private study, scholarship, or research". If a user makes a request for, or later uses, a photocopy or reproduction for purpose in excess of "fair use", that user may be liable for copyright infringement. This institution reserves the right to refuse to accept a copying order if, in its judgment, fulfillment of the order would involve violation of copyright law.

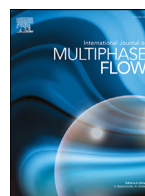
Interlibrary Loan Services: We Search the World for You...and Deliver!

Interlibrary Loan Services
The Florida State University
711 West Madison Street
Tallahassee, Florida 32306-1005

Lending the FSU Collection: 850.644.4171
James Elliott- ILL- lend@reserves.lib.fsu.edu

Borrowing for the FSU Community: 850.644.4466
Alicia Brown- ill@reserves.lib.fsu.edu

Odyssey: 128.186.59.120 Ariel: 146.201.65.22
Fax: 850.644.3329



Assembling a bubble-induced turbulence model incorporating physical understanding from DNS

Benjamin Magolan, Emilio Baglietto*

Department of Nuclear Science and Engineering, Massachusetts Institute of Technology, Cambridge, MA 02139, USA

ARTICLE INFO

Article history:

Received 25 July 2018

Revised 10 April 2019

Accepted 10 April 2019

Available online 11 April 2019

Keywords:

Bubble-Induced turbulence

$k - \varepsilon$ Models

Bubbly flow

Multiphase CFD

ABSTRACT

Bubble-induced turbulence (BIT) is a two-phase flow phenomenon characterized by complex interfacial interactions that fundamentally alter the resulting liquid turbulent kinetic energy distribution, budgets, and scales. Incorporating this complexity into a BIT model remains a formidable challenge, as existing two-equation BIT closures struggle with accurately predicting the turbulent kinetic energy and mean flow profiles. The present work assembles a BIT model that incorporates additional physical understanding into its formulation by leveraging insights garnered from experiments, DNS, and previous assessment. The model comprises new turbulent viscosity and time-scale formulations, in addition to optimized values for the modulation parameter, dissipation coefficient, and newly proposed turbulent viscosity multiplier. Improved model performance is demonstrated through simulation of air/water experimental cases and direct comparison with existing closures, which includes qualitative inspection of individual sets as well as quantitative assessment of the turbulent kinetic energy error distribution. Future work delving into momentum closure development, new experimental campaigns, and DNS parametric studies is motivated and linked to BIT model improvements.

Published by Elsevier Ltd.

1. Introduction

Two-phase bubbly flows arise in a wide array of engineering applications that include light-water nuclear reactors, thermal power plants, chemical separators, and bubble column reactors. Precise knowledge and understanding of the flow distribution is essential, as it leads to improved operation and safety in current systems, while further driving optimization and performance enhancement in next generation designs.

Multiphase Computational Fluid Dynamics (M-CFD) modeling and simulation techniques provide three-dimensional resolution of the complex flow structures inherent to these systems, granting insight into flow features that would otherwise not be accessible (or prohibitively expensive to obtain) via traditional experimental methods. This is an invaluable tool that aids the design process, however, such simulation predictions are only as valid as the underlying physical models.

Boiling, heat transfer, and chemical reaction mechanisms aside, the scope of purely hydrodynamic bubbly flow physics to consider and incorporate into the M-CFD framework is extensive. Countless previous efforts have been expended towards several key pillars

of research that include population balance, breakup/coalescence, as well as momentum and turbulent closure relations. The ensuing work navigates this intricate network of interdependencies by constraining focus to the topic of bubble-induced turbulence (BIT). By simplifying the scope to consider adiabatic, incompressible flow with constant fluid properties and bubble diameter, it is possible to concentrate focus on the physical understanding of BIT phenomena and assemble a model to better predict it.

1.1. Phenomena and mechanisms

Bubble-induced turbulence arises due to complex interactions between phases and leads to the modification of the liquid turbulent kinetic energy profile. Accurate resolution of the liquid turbulence is essential in many engineering applications, serving as a key driver in complex processes that include: chemical reaction rates in bubble column reactors; component fretting wear and mineral deposition in light-water nuclear reactors; and boiling heat transfer in steam generators. From an M-CFD perspective, BIT is critical for predicting the lateral phase distribution via solution of the interfacial forces; more specifically, turbulence directly impacts the turbulent dispersion force and indirectly affects the lift force through modification of the mean velocity gradient.

Examination of previous experimental and Direct Numerical Simulation (DNS) research endeavors reveals a complicated, incom-

* Corresponding author.

E-mail addresses: bmagolan@mit.edu (B. Magolan), emiliob@mit.edu (E. Baglietto).

plete, and nuanced picture of bubble-induced turbulence phenomena. As a primer to the discussion in Section 3, consider the following observations of two-phase turbulent distributions, energy budgets, and scales. First, while the liquid turbulent kinetic energy distribution is typically enhanced by comparison to its single-phase profile (augmentation), it can also be reduced (suppression) (Shawkat et al., 2008; Hosokawa and Tomiyama, 2009; Liu, 1989; Wang, 1985; Hibiki and Ishii, 1999; Hibiki et al., 2001; Serizawa et al., 1975), and in some instances, triggered in an otherwise laminar flow (pseudo-turbulence) (Hosokawa and Tomiyama, 2013; Nakoryakov et al., 1996). Second, the turbulent kinetic energy budget terms are fundamentally modified, resulting in a new quasi-equilibrium energy balance between production, dissipation, and interfacial transfer mechanisms, which has been observed experimentally (Lelouvetel et al., 2014; Shawkat and Ching, 2011) and through DNS (Santarelli et al., 2016; Magolan et al., 2017). Third, the relevant turbulent length- and time-scales of interest are dramatically altered, as evidenced by the -3 slope in energy spectra (e.g., Wang et al., 1990; Risso, 2011; Prakash et al., 2016; Brown and Bolotnov, 2016) as well as the considerable reduction in two-point correlation curves (e.g., Santarelli and Fröhlich, 2015; Shawkat et al., 2007; Wang et al., 1990).

1.2. Modeling techniques

Incorporating these physical mechanisms into a BIT model compatible within the Eulerian-Eulerian multiphase CFD framework remains a formidable challenge. The vast majority of BIT closures manifest as extensions to single-phase turbulence models, running the gamut in formulation complexity from algebraic turbulent viscosity models (e.g., Sato and Sekoguchi, 1975; Sato et al., 1981; Michiyoshi and Serizawa, 1986; Kataoka et al., 1993), to two-equation models (e.g., Lee et al., 1989; Lopez de Bertodano et al., 1994; Morel, 1997; Politano et al., 2003; Lahey, 2005; Troshko and Hassan, 2001; Rzehak and Krepper, 2013; Colombo and Fairweather, 2015; Ma et al., 2017), to Reynolds stress models, (e.g., Lopez de Bertodano et al., 1990; Colombo and Fairweather, 2015), and lastly, to spectral cascade transport models (Bolotnov et al., 2008a; 2008b). (The interested reader is referred to the work by Vaidheeswaran and Hibiki (2017) for a detailed review of these modeling strategies.) Since two-equation models have garnered the greatest exposure and successful application to industrial engineering problems, a BIT model leveraging this framework is assembled in the present work.

Two-equation BIT models manifest as additional source terms in two-equation turbulence models that describe the production (S_k) and dissipation (S_ε) of bubble-induced turbulence. Differences lie with the prescription of the constituent components that include the BIT time-scale (τ), modulation parameter (K_{BI}), and dissipation coefficient ($C_{\varepsilon B}$). The combination of these components impacts the solution of the $k-\varepsilon$ transport equations and thereby influences the predicted turbulent kinetic energy and mean flow profiles.

1.3. Assessment of existing closures

Existing BIT closures struggle with reliably predicting the liquid turbulent kinetic energy profile in addition to routinely worsening mean flow predictions. This is documented in Magolan et al. (2019), wherein the performance of several BIT models—Standard (no BIT), Sato et al. (1981), Troshko and Hassan (2001), Lahey (2005), Rzehak and Krepper (2013), Colombo and Fairweather (2015), and Ma et al. (2017)—was quantitatively assessed through simulation of the entire Liu (1989) air/water upward pipe flow experimental database using the OpenFOAM CFD

software. As part of that analysis, the connection between turbulence and the lateral redistribution forces was weakened through modification of the Burns et al. (2004) turbulent dispersion force. This decoupling approach ensures physically consistent volume fraction distributions for all closures, thereby enabling fair assessment and comparison of models.

Three important findings were highlighted in Magolan et al. (2019) that merit further investigation and incorporation into the model assembled in this work. First, turbulent viscosity (ν_t) plays a defining role in stabilizing the liquid velocity profile; while this statement is not surprising in the slightest, the paradoxical observation that improved turbulent kinetic energy predictions derive from a reduced turbulent viscosity profile, which subsequently worsens the liquid velocity prediction, suggests that the current definition of turbulent viscosity remains incomplete. Second, the time-scale (τ) impacts the shape of the turbulent kinetic energy profile as it migrates away from the wall; as such, a physically consistent time-scale should improve predictions by mitigating an artificial near-wall spike. Third, the ratio between the modulation parameter (K_{BI}) and dissipation coefficient ($C_{\varepsilon B}$) is a key driver that impacts the overall magnitude of the turbulent kinetic energy profile.

1.4. Approach to model formulation

The present work assembles a BIT model that incorporates physical understanding leveraged from experiments, DNS, and prior assessment into its formulation. The assembled model comprises new turbulent viscosity and time-scale formulations, as well as optimized values for the modulation parameter, dissipation coefficient, and newly proposed turbulent viscosity multiplier. Model assessment is performed via simulation of the entire Liu (1989) experimental database and direct comparison with several existing closures: Standard (no BIT), Troshko and Hassan (2001), Rzehak and Krepper (2013), Colombo and Fairweather (2015), and Ma et al. (2017).

More specifically, a new turbulent viscosity formulation is derived that accounts for the two-phase quasi-equilibrium energy balance between production, dissipation, and interfacial transfer. Additionally, a new bubble time-scale formulation is advanced based on physical intuition and two-point correlation statistics, wherein the distance between bubbles is considered the dominant length-scale. Lastly, parameter optimization is performed by physical classification of BIT turbulent regimes within the Liu (1989) experimental database: the modulation parameter is optimized in the augmentation dominated by bubble-induced production regime (low j_L , low j_G); the dissipation coefficient is optimized in the augmentation with enhanced dissipation regime (high j_L , high j_G); and the turbulent viscosity multiplier is optimized on the entire database to preserve generality and robustness.

During optimization and assessment, decoupled interfacial forces are utilized to facilitate correct and physically consistent prescription of the gas volume fraction and relative velocity distributions. This is a key strength of the assembled model, and further ensures that successive improvements to momentum closure relations will serve to improve turbulent kinetic energy predictions as well.

1.5. Structure of paper

Section 2 discusses the multiphase CFD framework leveraged during model assembly and assessment. This entails a concise review of the governing equations and decoupled momentum, turbulent, and bubble-induced turbulent closure relations, in addition to the computational modeling of the Liu (1989) experimental database in OpenFOAM. Section 3 reviews the relevant two-phase

turbulent phenomena that are incorporated into the new model. Discussion is organized into three categories of analysis that include turbulent distributions, energy budgets, and scales. [Section 4](#) assembles the model, detailing the construction of the new turbulent viscosity and time-scale formulations as well as the optimization of the modulation parameter, dissipation coefficient, and turbulent viscosity multiplier. [Section 5](#) assesses model performance via simulation of the entire [Liu \(1989\)](#) database and direct comparison with selected BIT closures. This includes qualitative inspection of predicted mean and turbulent profiles for individual sets in addition to quantitative examination of the resulting error distributions. [Section 6](#) concludes this work by summarizing model performance, identifying strengths and weaknesses, and advancing future avenues of research necessary for model improvement. Lastly, [Appendix A](#) integrates the assembled model into the hydrodynamic closures through recalibration of the turbulent dispersion force.

2. Multiphase CFD framework

The multiphase CFD framework leveraged during model assembly and assessment is briefly explored here. This includes discussion of the governing equations in addition to the computational modeling and simulation setup using the OpenFOAM CFD software.

2.1. Governing equations

For adiabatic, incompressible air/water flow with constant fluid properties, the Eulerian-Eulerian averaged equations for mass and momentum conservation simplify to (Drew and Passman, 1999; Yeoh and Tu, 2010; Ishii and Hibiki, 2011):

$$\frac{\partial(\alpha_k \rho_k)}{\partial t} + \frac{\partial(\alpha_k \rho_k U_{i,k})}{\partial x_i} = 0 \quad (1)$$

$$\begin{aligned} & \frac{\partial(\alpha_k \rho_k U_{i,k})}{\partial t} + \frac{\partial(\alpha_k \rho_k U_{i,k} U_{j,k})}{\partial x_i} \\ &= -\alpha_k \frac{\partial P}{\partial x_i} + \frac{\partial}{\partial x_j} [\alpha_k (\tau_{ij,k} + \tau_{ij,k}^{\text{Re}})] + \alpha_k \rho_k g_i + M_{i,k} \end{aligned} \quad (2)$$

Subscripts i and j denote Cartesian coordinate components, subscript k represents the phase (Gas or Liquid), α is volume fraction, ρ is density, \mathbf{U} is velocity, P is pressure, \mathbf{g} is gravity, and τ_{ij} is the laminar stress tensor. The volumetric interfacial force (\mathbf{M}) and turbulent Reynolds stress tensor (τ_{ij}^{Re}) require prescription of suitable momentum (Section 2.1.1), turbulent (Section 2.1.2), and bubble-induced turbulent (Section 2.1.3) closure relations to model, as reviewed in the following text.

2.1.1. Momentum closures

Drag (\mathbf{F}_D), lift (\mathbf{F}_L), turbulent dispersion (\mathbf{F}_{TD}), and wall lubrication (\mathbf{F}_{WL}) forces are modeled during assembly and assessment. The momentum exchange term (\mathbf{M}) represents the sum of these forces, with the sign convention defined with respect to the force exerted by the gas phase unto the liquid phase:

$$\mathbf{M} = \mathbf{F}_D + \mathbf{F}_L + \mathbf{F}_{TD} + \mathbf{F}_{WL} \quad (3)$$

Central to this work is the decoupling of the non-linear feedback between momentum and turbulent closure relations (see Fig. 1). By ensuring physically consistent relative velocity and volume fraction distributions, it is possible to concentrate focus on the optimization and assessment of the BIT model assembled in this work. This methodology includes directly prescribing the drag coefficient in addition to decoupling the lateral redistribution forces.

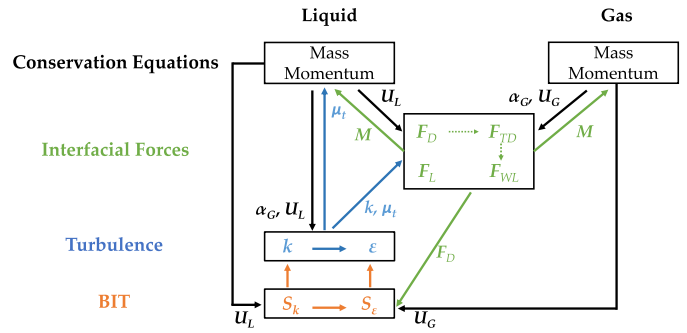


Fig. 1. Equation flow map illustrating the non-linear coupling between the governing equations, momentum closures, and turbulence models.

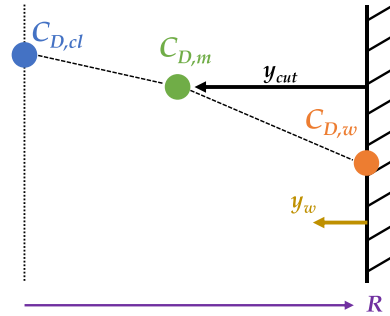


Fig. 2. Schematic of drag coefficient linear interpolation scheme.

Prescribing the Drag Coefficient

Drag is modeled in accordance with the classic formulation, where D_B represents the bubble diameter, and subscripts G and L denote the gas and liquid phases:

$$\mathbf{F}_D = \frac{3}{4} \frac{C_D}{D_B} \alpha_G \rho_L |\mathbf{U}_G - \mathbf{U}_L| (\mathbf{U}_G - \mathbf{U}_L) \quad (4)$$

The drag coefficient (C_D) is prescribed for all sets in the [Liu \(1989\)](#) database in order to accurately characterize the relative velocity (U_R) distribution. This is accomplished by directly specifying the drag coefficient at the wall ($C_{D,w}$), at the centerline ($C_{D,cl}$), and at a middle coordinate location ($C_{D,m}$) with a specified wall-normal (y_w) “cut-off” distance (y_{cut}), and linearly interpolating the values between these locations. (Note that these coefficients and the cut-off distance are unique values for each experimental case simulated.) The resulting expression is defined below and illustrated in [Fig. 2](#) for clarity:

$$C_D = \begin{cases} C_{D,w} + \left(\frac{C_{D,m} - C_{D,w}}{y_{cut}} \right) y_w, & y_w < y_{cut} \\ C_{D,m} + \left(\frac{C_{D,cl} - C_{D,m}}{R - y_{cut}} \right) (y_w - y_{cut}), & y_w > y_{cut} \end{cases} \quad (5)$$

This approach considerably improves the relative velocity predictions, as shown in Fig. 3 for the C_D and U_R profiles of set L5 from Liu (1989) (see Table 2). Experimental C_D values are estimated by equating the drag and buoyancy forces. As expected, prescribing the drag coefficient improves the aggregate prediction performance of these values, as evidenced in the error distribution plots for relative velocity in Fig. 4 and direct comparison with the Tomiyama et al. (1998) model.

Decoupling the Lateral Redistribution Forces

Lift is modeled using a constant coefficient (C_{l0}) equal to 0.03 that is damped to zero in the near-wall region using the [Shaver and Podowski \(2015\)](#) correction (Eq. (7)), where y_w represents the wall-normal distance. While this formulation is largely independent of BIT model, inevitable differences in the predicted turbulent viscosity act to modify the liquid velocity profile and thereby indirectly impact lift and the resulting volume fraction

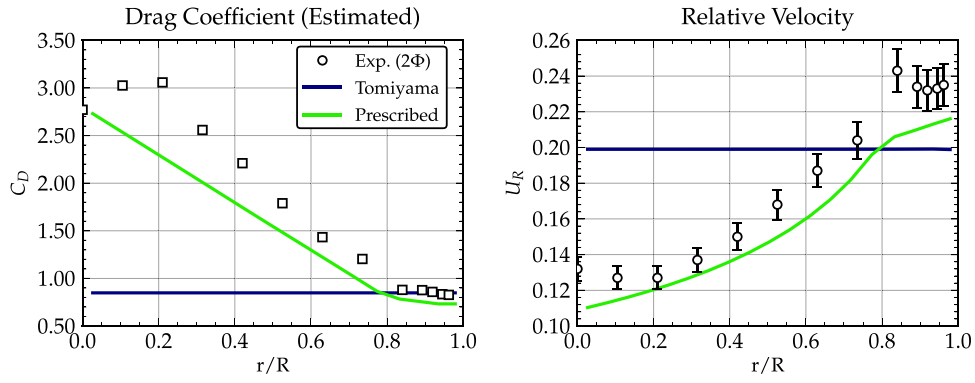


Fig. 3. Comparison of the predicted drag coefficient (C_D) and relative velocity (U_R) profiles for set L5 from the Liu (1989) database delivered by the Tomiyama et al. (1998) and directly prescribed drag coefficient models. Variables r and R denote distance from pipe centerline and total pipe radius, respectively.

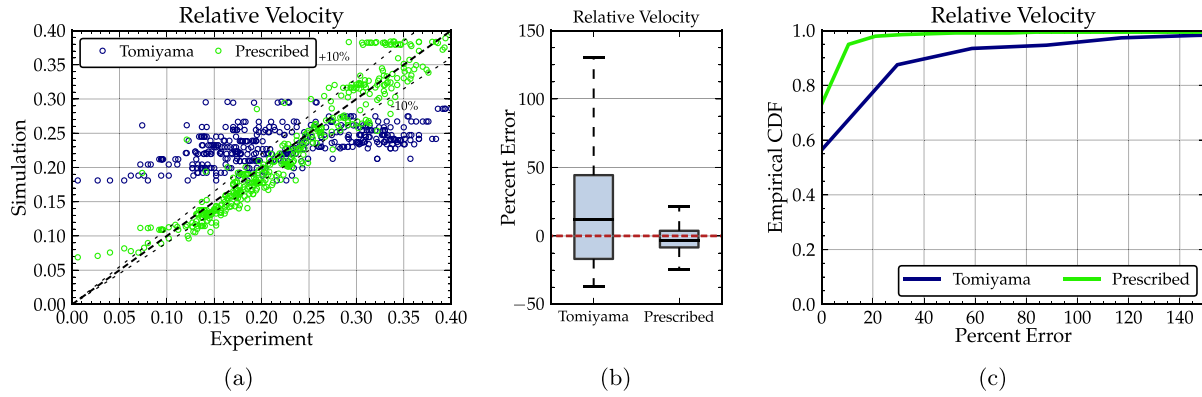


Fig. 4. Comparison of error distribution for relative velocity prediction delivered by the Tomiyama et al. (1998) and directly prescribed drag coefficient models for the entire Liu (1989) database visualized using (a) spread, (b) box, and (c) empirical CDF plots.

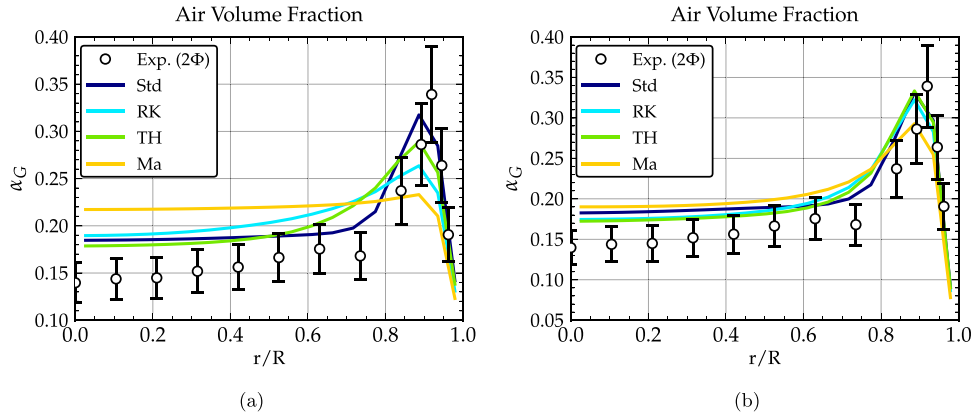


Fig. 5. Predicted gas volume fraction profile for set L19 from the Liu (1989) database using selected BIT closures with the turbulent dispersion model by (a) Burns et al. (2004) and (b) decoupled using Sato et al. (1981) bubble-induced turbulent viscosity.

profile (Eq. (6)). Nonetheless, the effect is minimal and no further adjustments to the lift force are applied.

$$\mathbf{F}_L = C_L \alpha_G \rho_L (\mathbf{U}_G - \mathbf{U}_L) \times (\nabla \times \mathbf{U}_L) \quad (6)$$

$$C_L = \begin{cases} 0, & y_w/D_B < 0.5 \\ C_{L0} \left[3 \left(\frac{2y_w}{D_B} - 1 \right)^2 - 2 \left(\frac{2y_w}{D_B} - 1 \right)^3 \right], & 0.5 < y_w/D_B < 1 \\ C_{L0}, & 1 < y_w/D_B \end{cases} \quad (7)$$

Turbulent dispersion by definition depends on turbulent quantities. This makes separate effects testing of BIT models intractable, as the BIT and turbulent dispersion models engage in a

non-linear feedback loop, whereby increased turbulence predictions increase the turbulent dispersion force, which flattens the radial volume fraction profile, thereby increasing drag and consequently the BIT production source term, further exacerbating the problem (recall Fig. 1). This leads to a dramatically over-powered turbulent dispersion force that flattens the radial gas volume fraction profile. This behavior is demonstrated through simulation of set L19 from Liu (1989) in Fig. 5a using the Std (no BIT), Treshko and Hassan (2001), Rzehak and Krepper (2013), and Ma et al. (2017) BIT models (summarized in Table 1) in conjunction with the Burns et al. (2004) turbulent dispersion model, where $\mu_{t,L}$ is the turbulent viscosity predicted by the two-equation turbulence

Table 1
Summary of Two-Equation BIT Models Compared Alongside New Model.

Author	Ref.	$\mu_{t,L}$	$C_{\mu B}$	K_{BI}	$C_{\varepsilon B}$	τ
Standard (no BIT)	Std	(12)	–	–	–	–
Troshko and Hassan (2001)	TH	(12)	–	1.0	$1.35 C_D$	$\frac{D_B}{ U_R }$
Rzehak and Krepper (2013)	RK	(12)	–	1.0	1.0	$\frac{D_B}{\sqrt{k}}$
Colombo and Fairweather (2015)	CF	(12)	–	0.25	1.0	$\frac{D_B}{\sqrt{k}}$
Ma et al. (2017)	Ma	(12)	–	$\min(0.18 \text{Re}_b^{0.23}, 1.0)$	$0.3 C_D$	$\frac{D_B}{ U_R }$
Present Work	NewModel	$C_{\mu B}$ (12)	$1.5 - 0.5 \exp(-10 \alpha_G)$	0.34	0.575	$\frac{D_B/\alpha_G^{1/3}}{ U_R }$

Table 2
Liu (1989) Database Summary of Experimental Set Mean Flow Parameters.

j_L^a	0.376			0.535			0.753			0.974			1.087			1.391		
j_G	Set	α_G	D_B	Set	α_G	D_B	Set	α_G	D_B	Set	α_G	D_B	Set	α_G	D_B	Set	α_G	D_B
0.347	L7	0.42	4.22	L14	0.34	4.11	L21	0.27	3.92	L28	0.21	3.81	L35	0.20	3.51	L42	0.17	3.28
0.293	L6	0.37	4.10	L13	0.31	3.90	L20	0.24	3.60	L27	0.19	3.53	L34	0.18	3.25	L41	0.15	3.05
0.23	L5	0.31	3.73	L12	0.23	3.55	L19	0.18	3.35	L26	0.15	3.29	L33	0.15	3.10	L40	0.12	3.02
0.18	L4	0.24	3.51	L11	0.20	3.30	L18	0.16	3.15	L25	0.12	3.07	L32	0.11	3.00	L39	0.10	2.90
0.112	L3	0.18	3.36	L10	0.14	3.12	L17	0.11	3.07	L24	0.08	2.96	L31	0.07	2.92	L38	0.06	2.82
0.067	L2	0.12	2.97	L9	0.09	2.86	L16	0.06	2.74	L23	0.05	2.60	L30	0.05	2.39	L37	0.04	2.68
0.027	L1	0.04	2.68	L8	0.03	2.60	L15	0.02	2.43	L22	0.02	2.28	L29	0.02	2.07	L36	0.01	1.97

^a Units: j_L, j_G [m/s]; α_G [-]; D_B [mm].

model for the liquid phase and $\sigma_{TD} = 1.0$:

$$\mathbf{F}_{TD} = \frac{3}{4} \frac{C_D}{D_B} \alpha_G |\mathbf{U}_G - \mathbf{U}_L| \left(\frac{1}{\sigma_{TD}} + \frac{1}{1 - \alpha_G} \right) \nabla \alpha_G \quad (8)$$

To remedy this issue, the bubble-induced turbulent viscosity formulation advanced by Sato et al. (1981)– $\nu_{t,BI} = 0.6 D_B |U_R|$ –is used in place of the shear-induced turbulent viscosity. Since this quantity depends solely on mean flow parameters (i.e., bubble diameter, D_B , and relative velocity between phases, U_R), the same value is predicted regardless of BIT model formulation, leading to consistent volume fraction predictions (Fig. 5b). The resulting formulation is defined in Eq. (9) with a value of 15 prescribed for σ_{TD} , which was determined through a sensitivity study to match performance with the Burns et al. (2004) formulation using the Std (no BIT) model:

$$\mathbf{F}_{TD} = \frac{3}{4} \frac{C_D}{D_B} \alpha_G |\mathbf{U}_G - \mathbf{U}_L| \frac{0.6 D_B |\mathbf{U}_G - \mathbf{U}_L| \rho_L}{15} \left(\frac{1}{\alpha_G} + \frac{1}{1 - \alpha_G} \right) \nabla \alpha_G \quad (9)$$

Wall lubrication also depends on turbulent viscosity and must be adjusted accordingly. Using the generalized formulation advanced by Lubchenko et al. (2018), the Sato et al. (1981) bubble-induced turbulent viscosity-corrected wall lubrication becomes:

$$\mathbf{F}_{WL} = \begin{cases} -\frac{3}{4} \frac{C_D}{D_B} |\mathbf{U}_G - \mathbf{U}_L| \frac{0.6 D_B |\mathbf{U}_G - \mathbf{U}_L| \rho_L}{15} \left(\frac{1}{\alpha_G} + \frac{1}{1 - \alpha_G} \right) \alpha_G \frac{1}{y_w} \frac{D_B - 2y_w}{D_B - y_w} \mathbf{n}, & y_w/D_B < 0.5 \\ 0, & y_w/D_B > 0.5 \end{cases} \quad (10)$$

This prescription of lateral redistribution forces ensures nearly consistent prediction of the radial gas volume fraction profile irrespective of BIT model for the entire Liu (1989) database. It is now possible to concentrate focus on turbulence modeling in order to assemble a new BIT closure.

2.1.2. Turbulence closures

Turbulence is modeled for the continuous (liquid) phase and neglected for the dispersed (gas) phase, as its contribution is assumed to be negligibly small due to the large density difference between phases. The liquid turbulent Reynolds stresses ($\tau_{ij,L}^{\text{Re}}$) are

modeled assuming linear proportionality to the mean velocity gradients of the flow:

$$\tau_{ij,L}^{\text{Re}} = \mu_{t,L} \left(\frac{\partial U_{i,L}}{\partial x_j} + \frac{\partial U_{j,L}}{\partial x_i} \right) - \frac{2}{3} I_{ij} \rho_L k_L \quad (11)$$

The turbulent viscosity ($\mu_{t,L}$) is the scaling factor, and is modeled through solution of two additional transport equations for the liquid turbulent kinetic energy (k_L) and the dissipation rate of liquid turbulent kinetic energy (ε_L):

$$\mu_{t,L} = C_\mu \frac{\rho_L k_L^2}{\varepsilon_L} \quad (12)$$

$$\frac{\partial(\alpha_L \rho_L k_L)}{\partial t} + \frac{\partial(\alpha_L \rho_L U_{i,L} k_L)}{\partial x_i} = \frac{\partial}{\partial x_j} \left[\alpha_L \left(\mu_L + \frac{\mu_{t,L}}{\sigma_k} \right) \frac{\partial k_L}{\partial x_j} \right] + \alpha_L (P_k - \rho_L \varepsilon_L) + S_k \quad (13)$$

$$\frac{\partial(\alpha_L \rho_L \varepsilon_L)}{\partial t} + \frac{\partial(\alpha_L \rho_L U_{i,L} \varepsilon_L)}{\partial x_i} = \frac{\partial}{\partial x_j} \left[\alpha_L \left(\mu_L + \frac{\mu_{t,L}}{\sigma_\varepsilon} \right) \frac{\partial \varepsilon_L}{\partial x_j} \right] + \alpha_L (C_{\varepsilon 1} P_k - C_{\varepsilon 2} \rho_L \varepsilon_L) \frac{\varepsilon_L}{k_L} + S_\varepsilon \quad (14)$$

The above equations represent the multiphase extension of the standard $k-\varepsilon$ model by Jones and Launder (1972), scaled by the liquid volume fraction (α_L) and incorporating two additional source terms (S_k and S_ε). Model coefficients are adopted from the single-phase equations: $\sigma_k = 1.0$, $\sigma_\varepsilon = 1.3$, $C_{\varepsilon 1} = 1.44$, $C_{\varepsilon 2} = 1.92$, and $C_\mu = 0.09$ (Launder and Sharma, 1974). Lastly, the production due to liquid shear (P_k) is modeled through the double inner product of the rate-of-strain tensor (S_{ij}):

$$P_k = 2 \mu_{t,L} S_{ij} S_{ij} \quad (15)$$

$$S_{ij} = \frac{1}{2} \left(\frac{\partial U_{i,L}}{\partial x_j} + \frac{\partial U_{j,L}}{\partial x_i} \right) \quad (16)$$

2.1.3. BIT Closures

The final terms in Eqs. (13) and (14) represent bubble-induced turbulent production (S_k) and dissipation (S_ε), which have the canonical modeling formulation first advanced by Lee et al. (1989):

$$S_k = K_{BI} \boldsymbol{\phi} \cdot \mathbf{U}_R \quad (17)$$

$$S_\varepsilon = C_{\varepsilon B} \frac{S_k}{\tau} \quad (18)$$

The BIT production term (S_k) comprises the dot product of the driving mechanism ($\boldsymbol{\phi}$)—which is the drag force (\mathbf{F}_D) for all models considered in the present work—with the relative velocity between phases (\mathbf{U}_R), scaled by a modulation parameter (K_{BI}) that controls the amount of interfacial turbulence transferred. The BIT dissipation term (S_ε) is constructed in an analogous fashion as was done for the shear dissipation term in the single phase ε equation, with the production term (S_k) divided by a characteristic time-scale (τ), scaled by a dissipation coefficient ($C_{\varepsilon B}$).

The majority of two-equation BIT models adhere to this general formulation, differing slightly with respect to their prescription of turbulent viscosity ($\mu_{t,L}$), driving mechanism ($\boldsymbol{\phi}$), modulation parameter (K_{BI}), time-scale (τ), dissipation coefficient ($C_{\varepsilon B}$), and formulation of the Reynolds stress tensor ($\tau_{ij,L}^{\text{Re}}$). The evolution of these terms for selected BIT models is rigorously examined in Magolan et al. (2019), and therefore for the sake of brevity, this discussion is omitted and only the components of existing closures that are assessed alongside the model assembled in this work are summarized in Table 1.

The model developed in this work adheres to the general framework for the BIT source terms. These terms are extended by incorporating additional physical understanding into the underlying formulation for the turbulent viscosity ($\mu_{t,L}$), time-scale (τ), modulation parameter (K_{BI}), dissipation coefficient ($C_{\varepsilon B}$), and newly proposed turbulent viscosity multiplier ($C_{\mu B}$).

2.2. Computational modeling in openfoam

Model assembly and assessment is performed in OpenFOAMv3.0 (Weller et al., 1998) using a custom modified version of the twoPhaseEulerFoam application, which simulates the transport of a two-phase mixture of continuous and dispersed phases using the Eulerian-Eulerian framework highlighted in the previous text. The Liu (1989) air/water upward pipe flow experimental database is simulated to support the optimization of parameters (Section 4.3) as well as to assess performance (Section 5). The experimental configuration and its computational modeling are briefly reviewed here for completeness.

2.2.1. Liu experimental database

The Liu (1989) experimental database comprises 42 sets of varying liquid and gas superficial velocities (j_L and j_G) as summarized in Table 2. The upward bubbly flow experiments were performed at atmospheric pressure and temperature conditions in a 38 mm diameter pipe, with radial profiles for mean (α_G , U_G , U_L , D_B) and turbulent (uu , vv , uv) quantities recorded 1.376 m downstream of the inlet ($L/D = 36.2$). Bubble quantities were measured using a dual-sensor resistivity probe and liquid quantities were obtained using both one- and two-dimensional hot-film anemometer probes.

The experimental liquid turbulent kinetic energy (k) is estimated in this work by assuming the radial and azimuthal turbulent

stresses to be approximately equal ($vv = ww$) based on similar observations reported by Wang (1985) and Wang et al. (1987). The experimental k profile is therefore defined as:

$$k = \frac{1}{2} (uu + 2vv) \quad (19)$$

2.2.2. Physical modeling

Density is constant for the continuous (water) phase, whereas it is modeled as an ideal gas for the dispersed (air) phase. Phase densities, viscosities, and surface tension are prescribed based on the reported pressure and temperature values from the experiments. Bubble diameter is modeled as a constant value of spherical shape, thereby foregoing any aspect ratio corrections. Lastly, only the liquid phase turbulence is modeled, as the gas phase contribution is assumed to be negligibly small due to the large density difference between the two phases.

2.2.3. Computational domain

The computational domain comprises a quarter-pipe geometry of 0.19 m radius and 1.6 m length. Computational mesh elements are constructed in CUBITv14, using a base size of 1 mm, 6 prism layers, a first cell thickness of 0.8 mm, and 100 cells in the axial direction. The computational mesh is displayed in Fig. 6.

Inlet boundary conditions are prescribed as uniform values using the set parameters listed in Table 2, with phase velocities computed as $U_k = j_k / \alpha_k$, a turbulent intensity of 0.1, and a turbulent viscosity ratio of 100. Outlet boundary conditions are set to atmospheric pressure and zero gradient for the remaining fluid properties. Symmetry boundary conditions are applied to the two rectangular planes that span the axial direction. Wall boundary conditions comprise no-slip for velocity, zero gradient for volume fractions and pressure, and the standard high-Reynolds turbulent wall functions (Launder and Spalding, 1974) for turbulent quantities. Lastly, the inlet boundary conditions are used to initialize the domain values at the start of each simulation.

2.2.4. Solution method

The pseudo steady-state solution is achieved by time-marching using the forward Euler scheme with a time-step corresponding to a CFL equal to 0.25. Each simulation is run for five seconds of physical time to ensure multiple domain flow-throughs and convergence to the steady-state profile. The unfortunately named PIMPLE algorithm controls the time-marching solution method. Regarding the pressure-velocity coupling scheme, 5 nOuterCorrectors, 3 pressure nCorrectors, and 0 under-relaxation nNonOrthogonalCorrectors are specified; likewise, for the volume fraction solver, 3 under-relaxation nAlphaSubCycles and 2 nAlphaCorr (ector) iterative steps are employed. Lastly, the faceMomentum switch is used to activate interpolation of interfacial forces to the cell faces when solving the momentum equation, which improves convergence and alleviates volume fraction checkerboarding.

On spatial discretization schemes, interpolation between the cell-center and cell-face is accomplished using the linear scheme. Gradients are calculated using the Gauss linear scheme. Divergence operations are performed using the Gauss scheme in combination with the following limiter schemes for the interpolated convective flux: vanLeer for volume fraction; limitedLinear 1 for scalar fields; limitedLinearV 1 for vector fields; and linear (no limiting) for stress terms. Surface normal gradients are computed using the uncorrected scheme. Lastly, laplacian operations are performed using the Gauss linear uncorrected scheme.

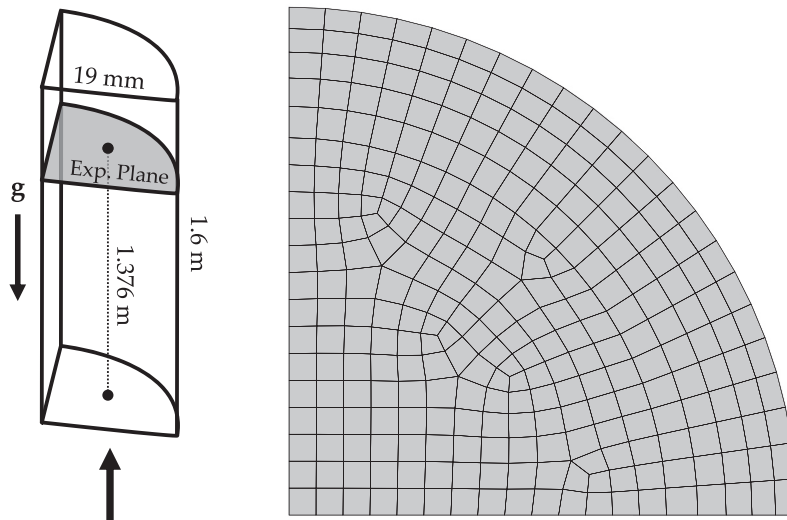


Fig. 6. Computational domain and mesh used for simulation of the Liu (1989) experimental database.

3. Two-Phase turbulence phenomena

Extending BIT modeling applicability and performance necessitates the incorporation of additional physical understanding into the underlying source term formulation that is defined in Eqs. (17)–(18) and listed in Table 1. Important two-phase turbulence phenomena obtained from previous experimental and DNS endeavors are briefly highlighted and examined with respect to three categories of analysis: turbulent distributions, turbulent kinetic energy budgets, and turbulent scales. These physical insights are connected with the specific BIT components (i.e., K_{BI} , $C_{\varepsilon B}$, μ_{tL} , and τ) that are assembled in Section 4.

3.1. Turbulent distributions

Modification of the liquid turbulent kinetic energy distribution in two-phase flow manifests in three forms: augmentation, suppression, and pseudo-turbulence. *Augmentation* is observed in the vast majority of cases, and is defined as the increase in turbulence levels by comparison to the single-phase profile for the same superficial liquid velocity (j_L). This phenomenon depends on several factors that include bubble deformability (e.g., Bunner and Tryggvason, 2003; Lu and Tryggvason, 2008; Feng and Bolotnov, 2017), bubble trajectory (Riboux et al., 2010), bubble curvature and resulting vortical wake structures (e.g., Leal, 1989; Batchelor, 2000), and gas volume fraction (e.g., as observed in experiments by Wang, 1985; Liu, 1989; Hibiki and Ishii, 1999; Hibiki et al., 2001; Shawkat et al., 2008).

Suppression is the local reduction of a given turbulence quantity that is observed in high j_L flows with gas volume fractions less than 5% (e.g., Serizawa et al., 1975; Wang, 1985; Liu, 1989; Hibiki and Ishii, 1999; Hibiki et al., 2001; Shawkat et al., 2008; Hosokawa and Tomiyama, 2009). This phenomenon has been attributed to a reduction in near-wall velocity gradients that weaken shear production (Lopez de Bertodano et al., 1994) as well as direct dissipation of BIT when the bubble diameter is of similar magnitude to the dissipation scales (Shawkat and Ching, 2011).

Pseudo-turbulence is the generation of fluid velocity fluctuations and liquid turbulent kinetic energy in an otherwise laminar or stagnant flow. This phenomenon is observed in low j_L pipe flow experiments (e.g., Nakoryakov et al., 1996; Hosokawa and Tomiyama, 2013) as well as bubble column experiments (e.g., Martínez Mercado et al., 2010; Mendez-Diaz et al., 2013; Prakash et al., 2016).

Experimental databases are instrumental in providing data for mean and turbulent distributions. Regrettably, only a very limited number of experimental databases exist that report sufficient mean (α_G , U_G , U_L , D_B) and turbulent (k , uu , vv , ww , uv) quantities from which it is possible to understand the complete picture of the two-phase flow distribution. Wang (1985) does not report bubble properties (D_B and U_G), which makes estimation of interfacial forces unclear. Serizawa et al. (1975), Hibiki and Ishii (1999), and Hibiki et al. (2001) only report the axial turbulent fluctuation (u), which makes estimation of k unclear. The Shawkat et al. (2008) large pipe diameter database is not considered due to challenges with reliably predicting the center-peaked void fraction distribution, a prerequisite for the construction of a new BIT model. Lastly, while Hosokawa and Tomiyama (2009) do indeed measure these quantities, it represents a small database comprising four sets with low gas volume fraction.

The Liu (1989) experiments (also documented in Liu and Bankoff, 1993a; 1993b) represent the only database that reports all necessary mean and turbulent quantities while simultaneously boasting a large volume of experimental sets spanning a broad range of volume fraction and turbulent regimes. It is therefore selected for BIT parameter optimization (i.e., K_{BI} , $C_{\varepsilon B}$, and $C_{\mu B}$), which is performed in Section 4.3. Experimental data is clearly needed and new research campaigns are strongly advised.

3.2. Turbulent kinetic energy budgets

The turbulent kinetic energy budget equation describes the balance and contribution of different mechanisms to the turbulent kinetic energy profile. In steady-state fully-developed two-phase flow, these balance equations simplify to the following form:

$$0 = \mathcal{P} + \varepsilon + \mathcal{C} + \mathcal{I} \quad (20)$$

These four terms are phase-weighted, ensemble averaged quantities that represent production (\mathcal{P}) due to liquid shear, dissipation (ε) due to fluctuating velocity gradients, transport (\mathcal{C}) due to viscous, turbulent, and pressure contributions, and interfacial transfer (\mathcal{I}) due to pressure and viscous fluctuations at the interface (Kataoka and Serizawa, 1989). In single-phase flow, there is an approximate balance between production and dissipation mechanisms in the bulk region. This observation is paramount to the derivation of the turbulent viscosity formulation (Eq. (12)). In two-phase flow, however, inspection of the resulting energy balance

reveals a complicated relationship triad between production, dissipation, and interfacial transfer mechanisms, which has been observed experimentally (e.g., [Shawkat and Ching, 2011](#); [Lelouvetel et al., 2014](#)) as well as via DNS analysis (e.g., [Santarelli et al., 2016](#); [Magolan et al., 2017](#)).

A new quasi-equilibrium energy balance between production, dissipation, and interfacial transfer mechanisms represents a fundamental modification to turbulence that must be modeled accordingly. This is accomplished through re-derivation of the turbulent viscosity formulation in [Section 4.1](#).

3.3. Turbulent scales

Turbulent eddies manifest in a multitude of sizes (or *scales*) that coexist, deform, and interact together. Several statistical analysis techniques can be applied to infer scale structure and subsequent modification in bubbly flow. Two important methods include examination of energy spectra and computation of two-point correlations.

Energy spectra portray the contribution of energy carried by eddies of a certain size–wavenumber (κ) or frequency (f)—which is obtained via Fourier transformation of the fluctuating velocity signal. A distinguishing feature of two-phase spectra is the modification of the characteristic $-5/3$ slope in the high frequency/wavenumber inertial and dissipation regions towards a value near -3 . This has been observed experimentally in pipe flow ([Michiyoshi and Serizawa, 1986](#); [Liu, 1989](#); [Wang et al., 1990](#)) and grid turbulence configurations ([Lance and Bataille, 1991](#); [Riboux et al., 2010](#); [Martínez Mercado et al., 2010](#); [Mendez-Diaz et al., 2013](#); [Prakash et al., 2016](#)), computed in DNS analyses ([Roghair et al., 2011](#); [Riboux et al., 2013](#); [Brown and Bolotnov, 2016](#)), as well as derived analytically ([Lance and Bataille, 1991](#); [Bolotnov et al., 2008a](#); [Risso, 2011](#)). The origin of the -3 slope is best elucidated by [Prakash et al. \(2016\)](#), wherein the authors examined the impact of the bubble frequency— $f_B = |\mathbf{U}_R|/(2\pi D_B)$ —on the resulting spectra; frequencies below this cutoff value (~ 10 Hz) exhibited a slope equal to $-5/3$, whereas frequencies above this cutoff displayed a slope equal to -3 . These spectra observations imply that there is an injection of energy on the scale of the bubble diameter (D_B) and frequency of bubble motion (f_B) that enhances dissipation.

Two-point correlations quantify the correlational relationship between two fluctuating velocity components ($u_i u_j$) that are separated by an interval in space or time. Bubbly flows evidence a considerable reduction in this correlational dependence, which has been observed experimentally ([Liu, 1989](#); [Wang et al., 1990](#); [Lance and Bataille, 1991](#); [Panidis and Papailiou, 2000](#); [Shawkat et al., 2007](#); [Panidis, 2011](#)) as well as computed in DNS analyses ([Santarelli and Fröhlich, 2015](#); [2016](#); [Magolan et al., 2017](#)). Most intriguing, inspection of the spatial two-point correlation data reported by [Santarelli and Fröhlich \(2015\)](#) reveals that turbulent scales depend on the distance between bubbles. The authors examined two DNS cases with the same bubble diameter, but of differing volume fraction: 0.29% and 2.14%. The reported stream-wise spatial two-point correlation for the higher volume fraction case exhibits a reduced correlation curve, which arises due to a smaller length-scale on account of the bubbles being closer together.

Examination of bubbly flow energy spectra and two-point correlation statistics yields two important conclusions regarding the dissipation of bubble-induced turbulence. First, the BIT dissipation time-scale (τ) depends on bubble characteristics that include its relative motion through the liquid. Second, the distance between bubbles is an important length-scale. Both of these physical insights are incorporated into the new time-scale formulation that is advanced in [Section 4.2](#).

4. Assembling the new model

The BIT model is assembled here by incorporating the physical understanding of two-phase turbulence phenomena highlighted in the previous section and further leveraging experience from prior assessment of existing closures in [Magolan et al. \(2019\)](#). The model comprises five components that include: a new turbulent viscosity (ν_t) formulation that is derived from the two-phase quasi-equilibrium turbulent kinetic energy balance; a new time-scale (τ) formulation based on bubble characteristics that is informed by energy spectra and two-point correlation analyses; and optimized formulations for the modulation parameter (K_{BI}), dissipation coefficient ($C_{\varepsilon B}$), and newly proposed turbulent viscosity multiplier ($C_{\mu B}$) that are obtained through simulation of specific turbulent regimes inherent to the [Liu \(1989\)](#) experimental database.

4.1. Turbulent viscosity (ν_t)

Assessment of existing bubble-induced turbulence models reveals the startling conclusion that improved liquid turbulent kinetic energy predictions come at the expense of worsened liquid velocity predictions ([Magolan et al., 2019](#)). This observation suggests that the current definition of turbulent viscosity ([Eq. \(12\)](#)) remains incomplete, which is affirmed through inspection of the turbulent kinetic energy balance in [Section 3.2](#). A turbulent viscosity formulation therefore accounting for the new quasi-equilibrium energy balance between production, dissipation, and interfacial transfer mechanisms requires derivation.

4.1.1. Multiphase equilibrium derivation

Recall that for single-phase flows, the turbulent kinetic energy budget equation simplifies to a balance between dissipation (ε) and shear production (\mathcal{P}) mechanisms in the bulk of the flow:

$$\varepsilon \approx \mathcal{P} \quad (21)$$

The single-phase turbulent viscosity formulation defined in [Eq. \(12\)](#)— $\nu_t = C_\mu k^2 / \varepsilon$ —is derived by multiplying both sides of [Eq. \(21\)](#) by ν_t , substituting in the expressions $\mathcal{P} = -uv(dU/dy)$ and $\nu_t = -uv/(dU/dy)$, relating $uv/k \approx 0.3$ using the log-layer stress-intensity relationship, and dividing ε to the right-hand side of the expression.

In two-phase flow, the quasi-equilibrium energy balance now includes the interfacial transfer (\mathcal{I}) mechanism:

$$\varepsilon \approx \mathcal{P} + \mathcal{I} \quad (22)$$

Applying the same methodology as before, let us multiply both sides of [Eq. \(22\)](#) by ν_t as well as substitute in the same single-phase expressions for shear production to achieve:

$$\nu_t \varepsilon = C_\mu k^2 + \nu_t \mathcal{I} \quad (23)$$

Grouping terms scaled by ν_t on the left-hand side and subsequently dividing this quantity to the right-hand side yields the following expression:

$$\nu_t = \frac{C_\mu k^2}{\varepsilon - \mathcal{I}} \quad (24)$$

4.1.2. Assessment

While turbulent viscosity is not commonly reported in experimental databases, it can be directly calculated from DNS statistics. With this in mind, the Lu/Tryggvason DNS data reported in [Magolan et al. \(2017\)](#) is reexamined in order to compute the theoretical turbulent viscosity using the expression:

$$\nu_t = \frac{-\overline{uv}}{(dU/dy)} \quad (25)$$

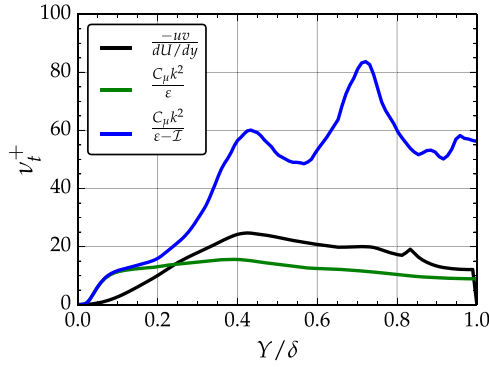


Fig. 7. Reexamination of Lu/Tryggvason DNS data reported in Magolan et al. (2017) to compute the normalized turbulent viscosity using theoretical expression (black curve, Eq. (25)), shear-induced model prediction (green curve, Eq. (12)), and new model formulation (blue curve, Eq. (24)). (For interpretation of the references to colour in this figure legend, the reader is referred to the web version of this article.)

The theoretical turbulent viscosity distribution (black curve, Eq. (25)) is overlaid with the profiles predicted using the shear-induced (green curve, Eq. (12)) and newly derived (blue curve, Eq. (24)) formulations. As observed in Fig. 7, there is a clear disparity between the theoretical distribution and the two modeled formulations, with the original shear-induced underpredicting and newly derived overpredicting. This discrepancy suggests that both formulations require further modification to match the theoretical turbulent viscosity distribution. Since additional DNS cases are necessary to explore this topic further, the model assembled in the present work adopts the simpler shear-induced turbulent viscosity formulation and proposes a turbulent viscosity multiplier ($C_{\mu B}$) to achieve the requisite scaling:

$$\nu_t = C_{\mu B} \frac{C_{\mu} k^2}{\epsilon} \quad (26)$$

The $C_{\mu B}$ parameter holds the requirement of reverting to the single-phase formulation in the absence of bubbles. Its formulation is optimized in Section 4.3 through simulation of the entire Liu (1989) experimental database.

4.2. Time-Scale (τ)

Existing BIT closures routinely deliver artificial spikes in the near-wall liquid turbulent kinetic energy profile (Magolan et al.,

2019). This result is attributable, in part, to the time-scale formulation, which impacts the shape of the turbulent kinetic energy profile as it migrates away from the wall. The new time-scale formulation advanced here addresses this aspect by leveraging the physical understanding from energy spectra and two-point correlation statistics that is outlined in Section 3.3, wherein a dissipation time-scale based on the bubble relative motion (U_R) and characteristic distance between bubbles (l) is constructed.

4.2.1. Derivation

There are several ways to derive the characteristic distance (l) between bubbles. The simplest approach is to consider a sphere of unit volume fraction with a bubble located at the origin. Other methods include considering a unit lattice arrangement of bubbles and assuming a certain packing orientation, such as simple cubic or body-centered cubic. In all cases the result is a dependency on bubble diameter divided by the cube root of the local volume fraction ($D_B/\alpha_G^{1/3}$). Implicit in these derivations are a host of assumptions regarding bubble dynamics that include uniform spacing, non-deformability (spherical shape), and non-preferential alignment.

With these considerations in mind, the simplest length-scale ($D_B/\alpha_G^{1/3}$) is selected with the implicit assumption that further calibration is performed through optimization of the dissipation coefficient ($C_{\epsilon B}$) in Section 4.3. The resulting time-scale formulation incorporated into the new model is therefore defined as:

$$\tau = \frac{(D_B/\alpha_G^{1/3})}{|U_R|} \quad (27)$$

4.2.2. Assessment

For a fixed relative velocity (U_R), increasing the bubble diameter (D_B) also increases the time-scale; conversely, for fixed D_B , increasing $|U_R|$ reduces the time-scale. Further, in the limit of zero gas volume fraction (α_G), the time-scale approaches infinity (causing BIT dissipation to go to zero); correspondingly, as α_G approaches unity, the time-scale asymptotes to the bubble time-scale ($D_B/|U_R|$) that is prescribed in the models by Troshko and Hassan (2001) and Ma et al. (2017) that are summarized in Table 1. With everything else equal (e.g., K_{BI} , $C_{\epsilon B}$, interfacial forces), the $D_B/|U_R|$ time-scale yields a smaller time-scale and therefore will predict greater dissipation everywhere in the domain.

As a practical example demonstrating the impact of the BIT time-scale, consider set L18 from the Liu (1989) database (see Table 2 for flow parameters) for which three BIT model prototypes employing the following time-scales are examined:

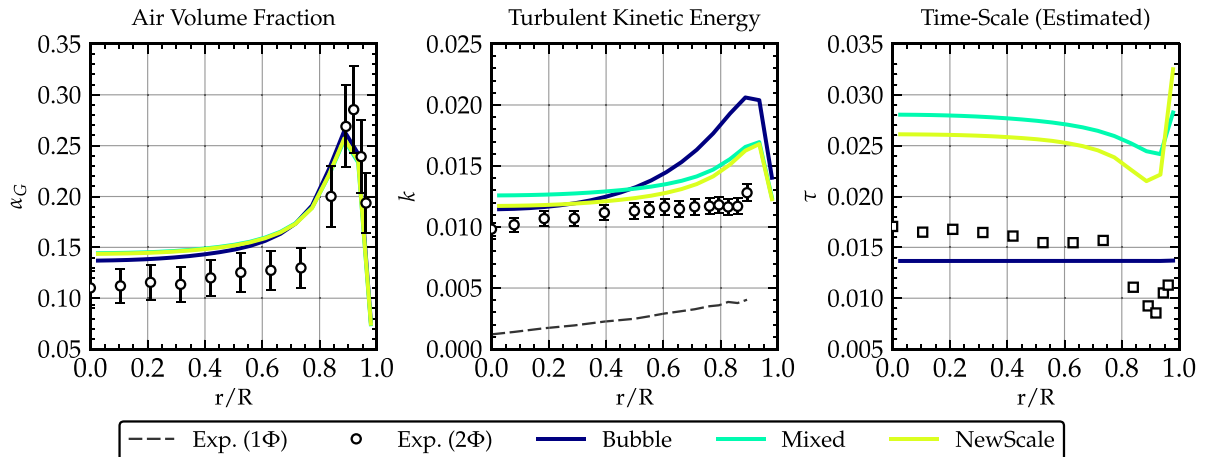


Fig. 8. Impact of time-scale formulation on resulting gas volume fraction, liquid turbulent kinetic energy, and time-scale profiles for set L18 from the Liu (1989) database. The experimental time-scale profile is estimated as the reciprocal of the reported radial bubble frequency.

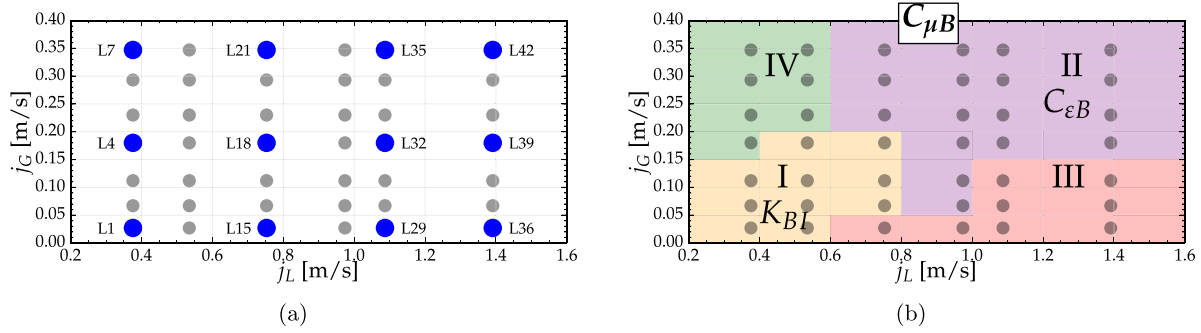


Fig. 9. The Liu (1989) experimental database (a) superficial velocity ($j_k = U_k \alpha_k$) flow map is (b) partitioned into four turbulent regimes in order to optimize K_{BI} , $C_{\epsilon B}$, and $C_{\mu B}$. The enlarged markers colored in blue denote sets that are qualitatively examined through inspection of predicted profiles in Section 5.1. Turbulent regimes correspond to (I) augmentation dominated by bubble-induced production, (II) augmentation with enhanced dissipation, (III) suppression, and (IV) slug/churn pseudo-turbulence. (For interpretation of the references to colour in this figure legend, the reader is referred to the web version of this article.)

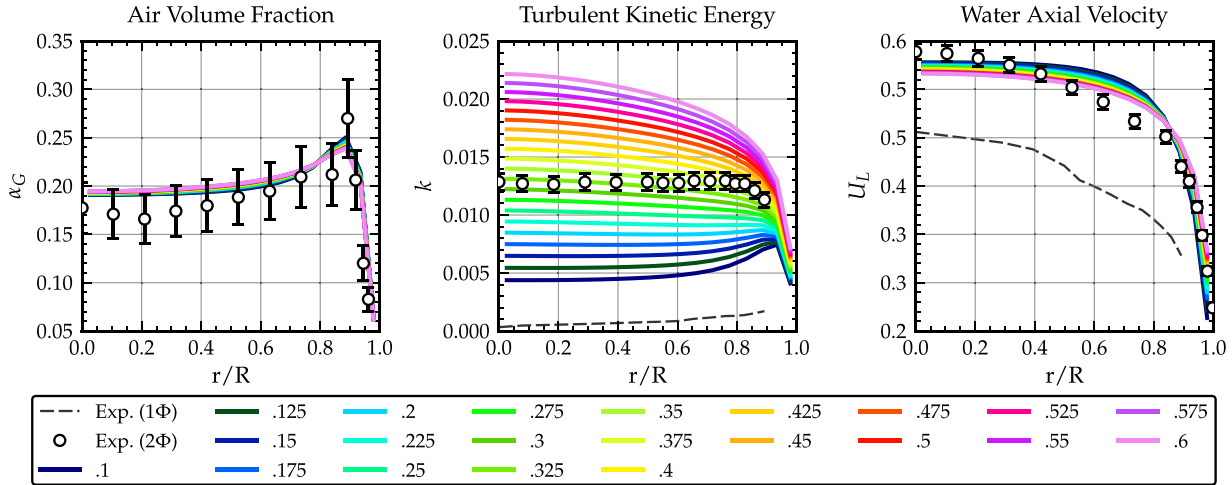


Fig. 10. Optimizing K_{BI} : Demonstration of approach on set L3 from Liu (1989) experimental database through examination of volume fraction, turbulent kinetic energy, and liquid velocity profiles. K_{BI} is varied from 0.1 to 0.6 in increments of 0.025.

Bubble ($D_B/|U_R|$), Mixed ($D_B/k^{1/2}$), and NewScale ($(D_B/\alpha_G^{1/3})/|U_R|$). For these simulations, the dissipation coefficient ($C_{\epsilon B}$) is fixed to 0.5 and the modulation parameter (K_{BI}) is calibrated to achieve similar turbulent kinetic energy values at the pipe center-line ($r/R = 0$): Bubble, $K_{BI} = 0.7$; Mixed, $K_{BI} = 0.35$; NewScale, $K_{BI} = 0.35$.

The resulting gas volume fraction (α_G), liquid turbulent kinetic energy (k), and time-scale (τ) profiles are plotted in Fig. 8 (note that the experimental time-scale is estimated as the reciprocal of the reported bubble frequency). Comparison of the NewScale and Bubble time-scales demonstrates improved prediction performance for turbulent kinetic energy. The use of the constant Bubble time-scale does not match the trends properly, as insufficient dissipation is provided near the wall, leading to the overprediction of k near the wall.

Interestingly, the NewScale and Mixed time-scales perform similarly well with predicting k . This arises from similar τ profiles (both in magnitude and shape), which attain a minimum in the near-wall region and increase towards the pipe center-line. Dissipation is enhanced near the wall due to the increase in α_G and k for the NewScale and Mixed time-scales, respectively; this exhibits the favorable trend of reducing the near-wall artificial spike in k . Likewise, when approaching the pipe center-line, the α_G and k profiles both decrease, which causes τ to level off for both models. These observations further confirm that predicting a favorable time-scale shape is essential for accurate resolution of the turbulent kinetic energy profile.

4.3. Parameter optimization

The ratio between the modulation parameter (K_{BI}) and dissipation coefficient ($C_{\epsilon B}$) impacts the overall magnitude of the predicted liquid turbulent kinetic energy profile (Magolan et al., 2019). These two parameters, in addition to the newly proposed turbulent viscosity multiplier, $C_{\mu B}$, are constructed herein by leveraging the insights of turbulent distributions that are reviewed in Section 3.1. Parameter optimization is accomplished through simulation of the Liu (1989) database and calibration with specific bubble-induced turbulent regimes. This approach incorporates the turbulent viscosity (Eq. (26)) and time-scale (Eq. (27)) formulations advanced in the previous text in addition to using the interfacial force decoupling methodology outlined in Section 2.1.1 to ensure physically consistent volume fraction and relative velocity distributions.

4.3.1. Approach

As highlighted in Section 3.1, it is rare to find an experimental database that reports sufficient mean (α_G , U_G , U_L , D_B) and turbulent (k , uu , vv , ww , uv) quantities spanning a broad range of turbulent regimes to support rigorous model assembly, calibration, and assessment. Liu (1989) is the only database that satisfies these criteria, and is therefore selected for parameter optimization.

A flow map plotting the liquid and gas superficial velocities (j_L and j_G) for the entire Liu (1989) database is depicted in Fig. 9a for the experimental sets summarized in Table 2. The flow map is partitioned into four bubble-induced turbulent regimes that

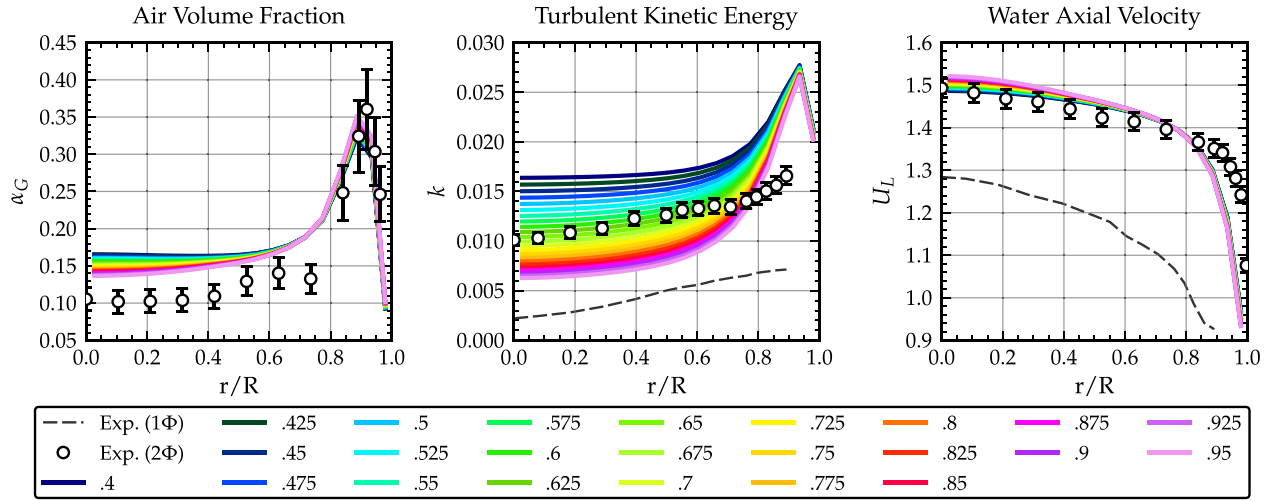


Fig. 11. Optimizing C_{EB} : Demonstration of approach on set L34 from Liu (1989) experimental database through examination of volume fraction, turbulent kinetic energy, and liquid velocity profiles. C_{EB} is varied from 0.4 to 0.95 in increments of 0.025.

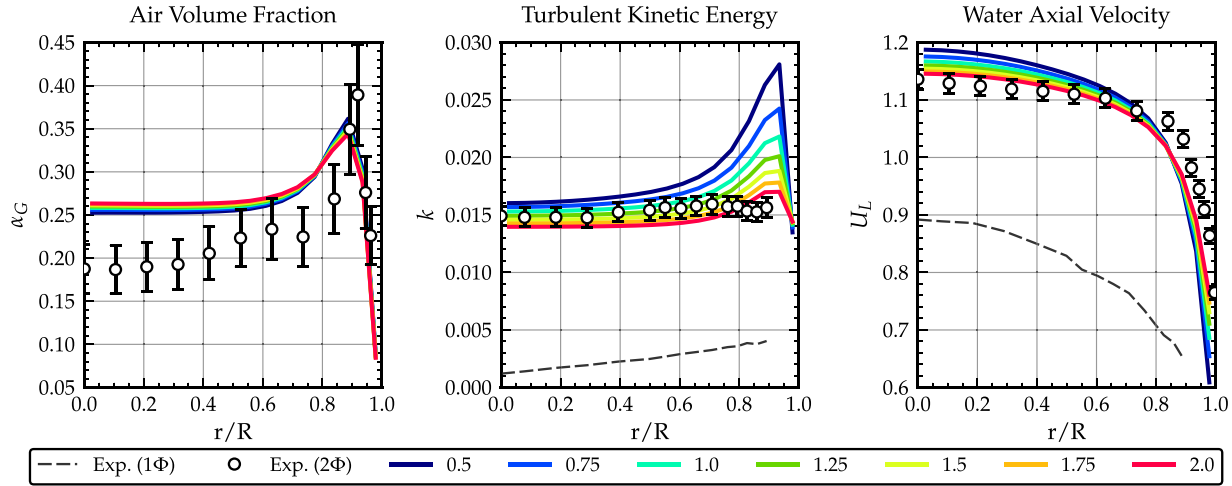


Fig. 12. Optimizing $C_{\mu B}$: Demonstration of approach on set L20 from Liu (1989) experimental database through examination of volume fraction, turbulent kinetic energy, and liquid velocity profiles. $C_{\mu B}$ is varied from 0.5 to 2.0 in increments of 0.5.

correspond to (I) augmentation dominated by bubble-induced production, (II) augmentation with enhanced dissipation, (III) suppression, and (IV) slug/churn pseudo-turbulence (Fig. 9b).

The modulation parameter (K_{BI}) is optimized on the first regime. This domain is characterized by low gas volume fraction, low liquid velocity flows that yield relatively flat radial turbulent kinetic energy (k) profiles. In this region there exists comparatively low levels of shear production, and consequently, the majority of BIT production derives from the bubble agitation.

The dissipation coefficient (C_{EB}) is optimized on the second regime. This domain is characterized by high gas volume fraction, high liquid velocity flows with k profiles that peak near the wall and decay towards the pipe center-line. In this region there is enhanced dissipation due to the combination of high bubble frequencies and greater bubble deformability.

The turbulent viscosity multiplier ($C_{\mu B}$) is optimized on all four regimes to preserve generality and robustness. This term must revert to unity in the absence of bubbles to recover the single-phase turbulent viscosity formulation.

4.3.2. Modulation parameter (K_{BI})

The modulation parameter is optimized on BIT regime I (Fig. 9b) where the majority of augmentation derives from the

Table 3
Optimal K_{BI} Values for Liu (1989) Sets in Bubble Production Turbulent Regime.

Set	$K_{BI,opt}$	Set	$K_{BI,opt}$	Set	$K_{BI,opt}$
				L19	0.325
				L18	0.3
L3	0.325	L11	0.375	L17	0.3
L2	0.325	L10	0.475	L16	0.325
L1	0.325	L9	0.4		
		L8	0.275		

bubble motion and subsequent liquid agitation. The dissipation coefficient (C_{EB}) is fixed to 0.5 with K_{BI} varied from 0.1 to 0.6 in increments of 0.025. The K_{BI} value that minimizes the L2 error for the predicted k in the bulk ($r/R < 0.8$) is selected as the optimal value for a given set. The resulting gas volume fraction, turbulent kinetic energy, and liquid velocity distributions for set L3 are illustrated in Fig. 10 as a demonstration of this process. Optimal values for each set are listed in Table 3, the average of which is adopted as the K_{BI} model formulation:

$$K_{BI} = 0.34 \quad (28)$$

Table 4
Optimal $C_{\varepsilon B}$ Values for Liu (1989) Sets in Enhanced Dissipation Turbulent Regime.

Set	$C_{\varepsilon B, \text{opt}}$	Set	$C_{\varepsilon B, \text{opt}}$	Set	$C_{\varepsilon B, \text{opt}}$	Set	$C_{\varepsilon B, \text{opt}}$
L21	0.75	L28	0.6	L35	0.825	L42	0.5
L20	0.7	L27	0.6	L34	0.65	L41	0.425
L19	0.55	L26	0.475	L33	0.5	L40	0.425
L18	0.575	L25	0.5	L32	0.5	L39	0.625

4.3.3. Dissipation coefficient ($C_{\varepsilon B}$)

With the formulation for K_{Bl} established, the dissipation coefficient is optimized on BIT regime II (Fig. 9b) where it is surmised that dissipation effects are enhanced due to greater concentrations of deformable bubbles. The dissipation coefficient is varied from 0.4 to 0.95 in increments of 0.025. As with the modulation parameter, the $C_{\varepsilon B}$ value that minimizes the L2 error for k in the bulk ($r/R < 0.8$) is selected as the optimal value for that particular set. The resulting gas volume fraction, turbulent kinetic energy, and liquid velocity distributions for set L34 are illustrated in Fig. 11 as a demonstration of this process. Optimal values for each set are listed in Table 4, the average of which is incorporated into the $C_{\varepsilon B}$ model formulation:

$$C_{\varepsilon B} = 0.575 \quad (29)$$

4.3.4. Turbulent viscosity multiplier ($C_{\mu B}$)

As chronicled during derivation of the new turbulent viscosity formulation (Section 4.1), a turbulent viscosity multiplier is neces-

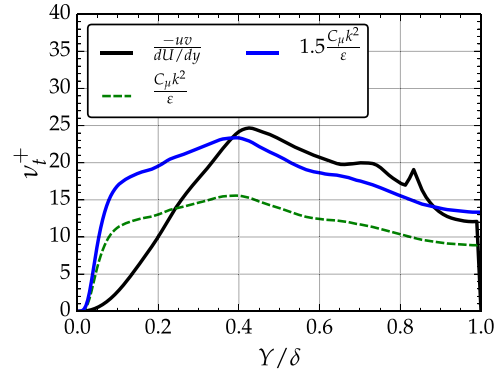


Fig. 13. Reexamination of the Lu/Tryggvason turbulent viscosity profiles reveals that $C_{\mu B} = 1.5$ matches the DNS data well.

sary to accommodate the enhanced turbulent viscosity evidenced in the Lu/Tryggvason DNS data (Fig. 7). This parameter is formulated through simulation of the entire Liu (1989) database (Fig. 9b) using the optimized K_{Bl} and $C_{\varepsilon B}$ coefficients developed above. The $C_{\mu B}$ multiplier is varied from 0.5 to 2.0 in increments of 0.25 and the L2 error for k is examined for each set. Simulation predictions for gas volume fraction, turbulent kinetic energy, and liquid velocity for set L20 are plotted in Fig. 12 as a demonstration of this procedure. Increasing $C_{\mu B}$ has the favorable attribute of reducing the turbulent kinetic energy spike in the near-wall region. This

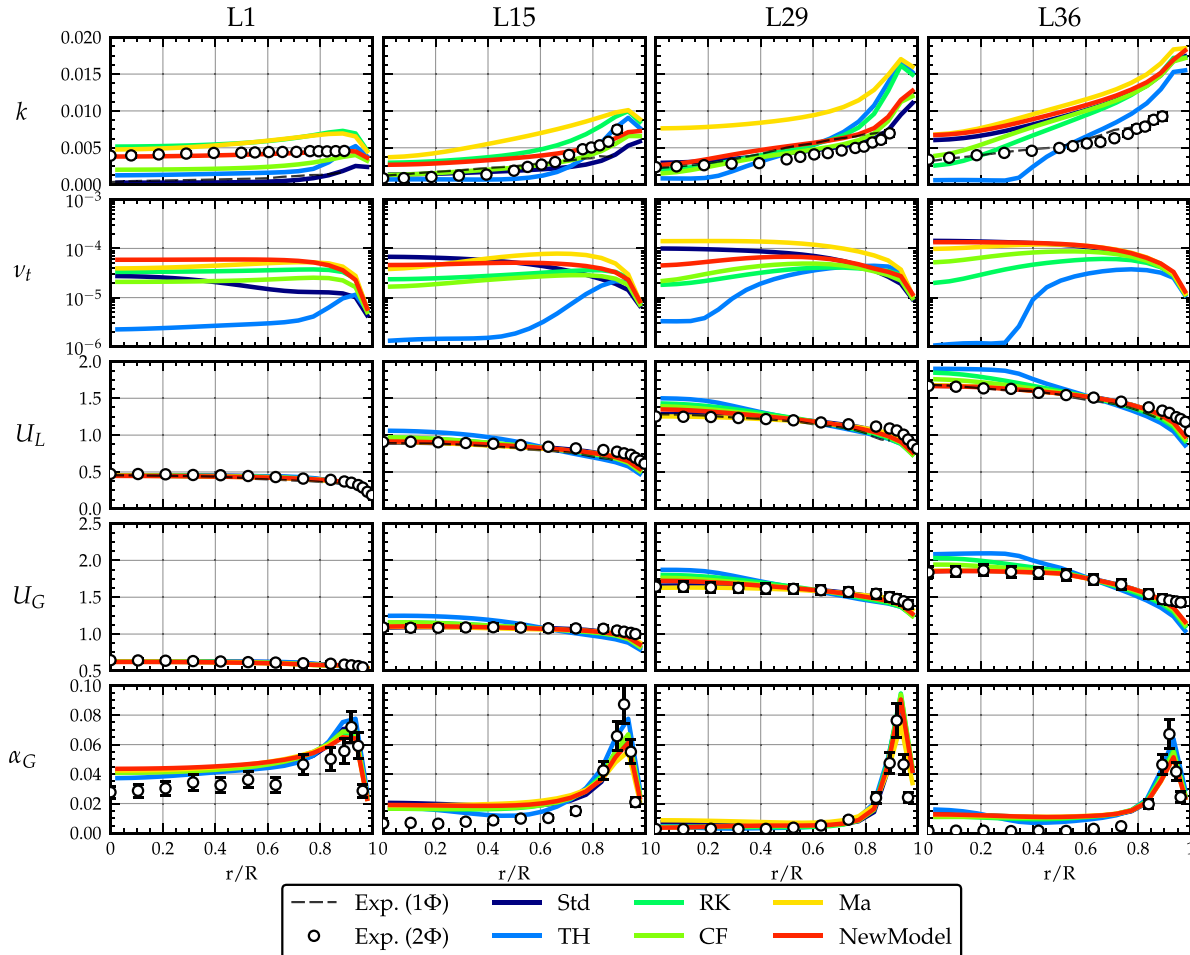


Fig. 14. Assembled BIT Model Assessment: Individual sets examining predicted mean and turbulent quantities for selected sets from first row ($j_c = 0.027$ m/s) of Liu (1989) experimental database. Traversing rightwards denotes increasing j_L (0.376, 0.753, 1.087, and 1.391 m/s).

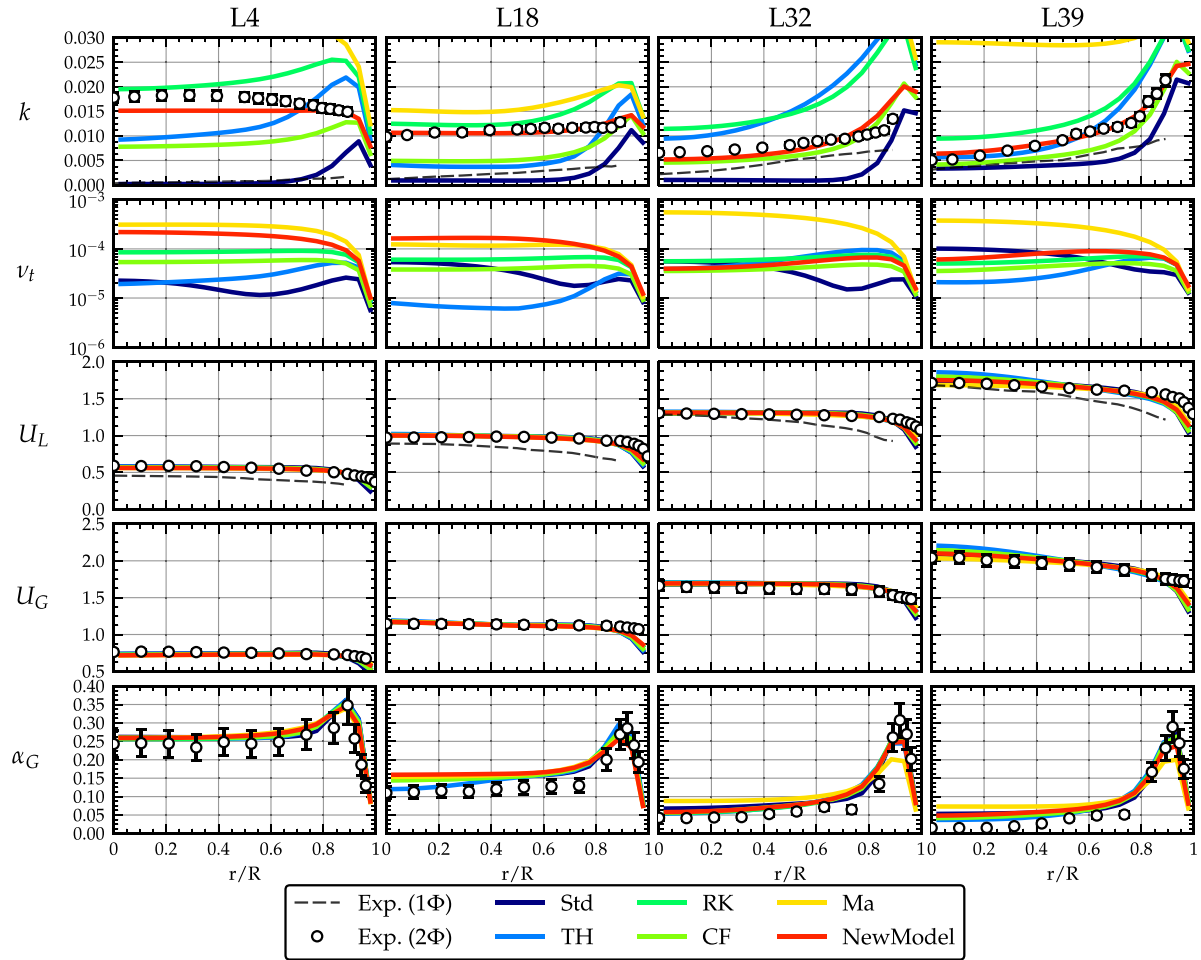


Fig. 15. Assembled BIT Model Assessment: Individual sets examining predicted mean and turbulent quantities for selected sets from **fourth** row ($j_G = 0.18$ m/s) of Liu (1989) experimental database. Traversing rightwards denotes increasing j_L (0.376, 0.753, 1.087, and 1.391 m/s).

occurs because the near-wall velocity prediction is shifted upwards, which thereby reduces shear production due to the shallower velocity gradient. For the simulated database the optimal $C_{\mu B}$ is observed to increase with increasing volume fraction. With this trend in mind, a multiplier ranging between 1.0 to 1.5 is developed using an exponential function related to local volume fraction (α_G) through the following formulation:

$$C_{\mu B} = 1.5 - 0.5 \exp(-10 \alpha_G) \quad (30)$$

A scaling on the order of 50% is in the realm of possibility. This is evidenced through reexamination of the Lu/Tryggvason DNS data, whereby setting $C_{\mu B} = 1.5$ yields a turbulent viscosity prediction that matches the profile quite nicely (Fig. 13). Additional DNS efforts to further investigate and improve this formulation are highly encouraged.

4.4. Model summary

The assembled bubble-induced turbulence model is summarized in the final row of Table 1. Its construction allows for automatic reversion to the single-phase $k - \varepsilon$ equations in the limit of zero gas volume fraction. This is implicit in the S_k and S_ε source term formulations, which are scaled by the volume fraction. The exponential function defining the turbulent viscosity multiplier ($C_{\mu B}$) in Eq. (30) ensures that its value scales to unity in the limit of zero volume fraction, allowing for recovery of the single-phase turbulent viscosity formulation.

5. Model assessment

The model assembled in the previous section is assessed through simulation of the entire Liu (1989) database and direct comparison with the Std (no BIT), Troshko and Hassan (2001), Rzehak and Krepper (2013), Colombo and Fairweather (2015), and Ma et al. (2017) models that are summarized in Table 1. All simulations employ the interfacial force decoupling methodology described in Section 2.1.1 to ensure physically consistent volume fraction and relative velocity distributions.

Three categories of analysis are applied to assess model performance. This includes qualitative inspection of selected field quantities (i.e., α_G , U_G , U_L , v_t , and k) for a subset of cases (represented by the enlarged blue markers in Fig. 9a), visualization of the error spread for k , and quantification of the error distribution for k through use of box plots and empirical cumulative distribution function plots.

5.1. Individual sets

Four sets from the first, fourth, and seventh rows from the Liu (1989) experimental database (Fig. 9a) are plotted in Figs. 14–16, respectively. These cases correspond to low ($j_G = 0.027$ m/s), moderate ($j_G = 0.18$ m/s), and high ($j_G = 0.347$ m/s) gas superficial velocity flows wherein suppression, augmentation, and slug/churn pseudo-turbulent phenomena arise. Each column represents an experimental set, where traversing rightwards denotes increasing

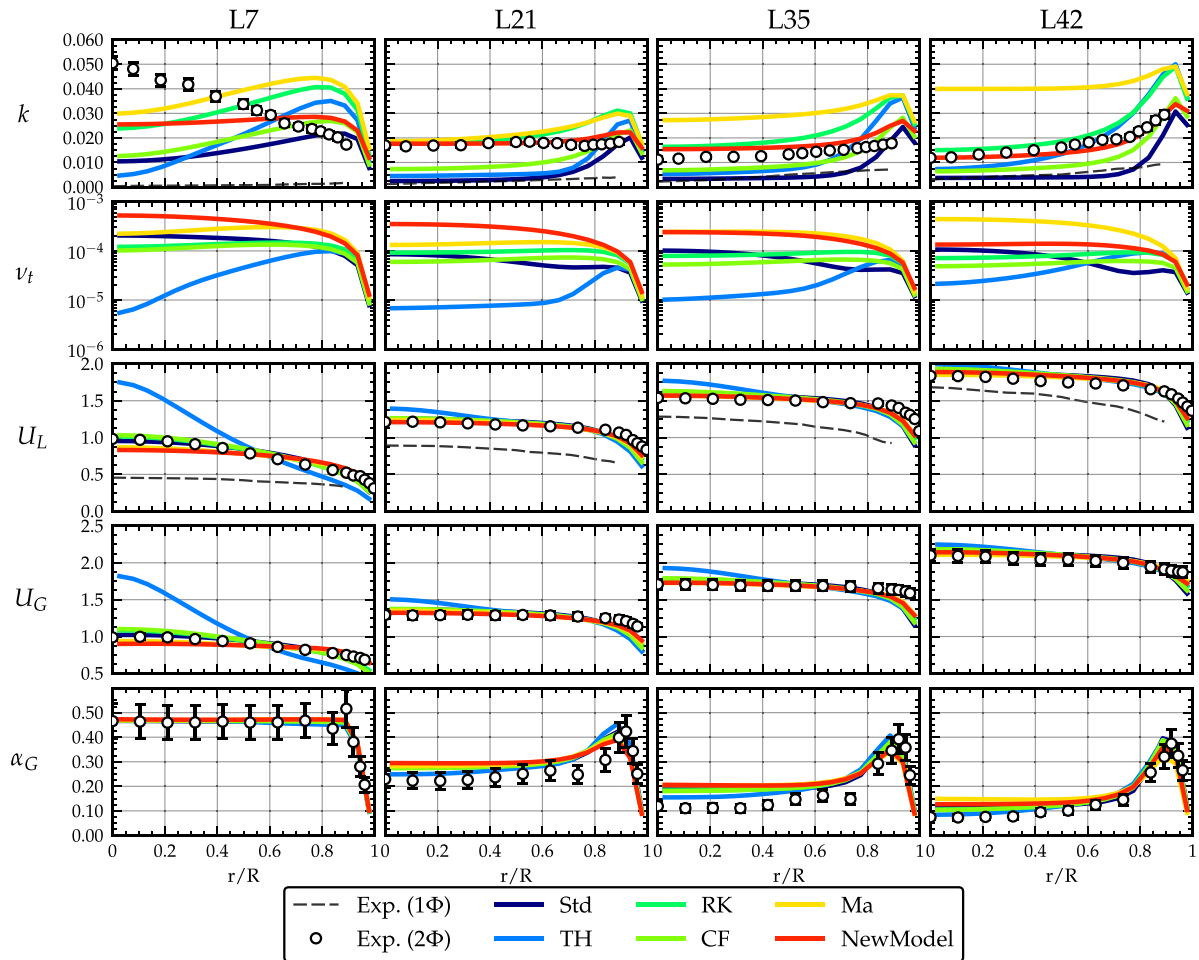


Fig. 16. Assembled BIT Model Assessment: Individual sets examining predicted mean and turbulent quantities for selected sets from **seventh** row ($j_L = 0.347$ m/s) of Liu (1989) experimental database. Traversing rightwards denotes increasing j_L (0.376, 0.753, 1.087, and 1.391 m/s).

liquid superficial velocity: $j_L = 0.376, 0.753, 1.087$, and 1.391 m/s. Each row plots the radial distribution of desired field quantities at the measurement plane that include the gas volume fraction (α_G), stream-wise phase velocities (U_G , U_L), turbulent viscosity (ν_t), and turbulent kinetic energy (k). Axes are scaled identically to facilitate direct comparison of distributions between sets. When applicable, solid gray curves and circle marker points with error bars denote the single- and two-phase experimental measurements, respectively.

Despite the decoupling strategy adopted to stabilize the drag and lateral redistribution forces, the examined models exhibit minor variations for the predicted mean flow profiles. In general, the gas volume fraction (row 5), gas velocity (row 4), and liquid velocity (row 3) distributions are slightly overpredicted in the bulk and underpredicted near the wall. The TH model evidences the greatest overprediction for the bulk liquid velocity, followed by RK, CF, and then Ma; the assembled “NewModel” performs quite well with predicting the center-line values in the majority of cases. Interestingly, since the TH model overpredicts liquid velocity, it is characterized by a slightly stronger lift force (due to a larger velocity gradient), which forces more void to the wall and yields the comparatively better gas volume fraction distribution.

Turbulent viscosity (row 2) is the culprit for these deviations in the center-line liquid velocity profile. As evidenced in columns 3 and 4, TH consistently delivers the lowest turbulent viscosity prediction, followed by CF and RK, with Std, Ma, and the NewModel clustered together (the exact opposite trend as observed for U_L).

Greater turbulent viscosity signifies a more turbulent flow, which acts to flatten the velocity profile. Columns 1 and 2 represent low j_L flow rates, wherein bubble dynamics dominate and mask the impact of turbulent viscosity; however, for the higher j_L flow conditions characteristic of columns 3 and 4, shear production mechanisms at the wall become increasingly more important. These differences in model performance depend on the turbulent viscosity formulation as well as the combined effects of the modulation parameter, dissipation coefficient, and time-scale on the resultant solution of the turbulent kinetic energy (k) and dissipation (ϵ) transport equations (Eqs. (13) and (14)).

Turbulent kinetic energy (row 1) predictions are quite varied with model performance and depend on the two-phase turbulence phenomena. Suppression is observed in the bottom right corner of the superficial velocity flow map (Fig. 9b) for sets L15, L29, and L36 (Fig. 14); augmentation is observed in the bottom left corner for set L1 (Fig. 14), all sets in the fourth row (Fig. 15), and sets L21, L35, and L42 in the top right corner (Fig. 16); and lastly, slug/churn pseudo-turbulence is observed for set L7 in the top left corner (Fig. 16). The experimental profile is generally quite flat in the first two columns, which demonstrates that bubble dynamics are the primary source of liquid turbulent kinetic energy production; however, in columns 3 and 4 the profiles exhibit a decay away from a maximum value near the wall, indicating that shear production mechanisms become increasingly important. Overall, the Std, TH, and CF models routinely underpredict the turbulent kinetic energy profile while RK and Ma overpredict it. The NewModel

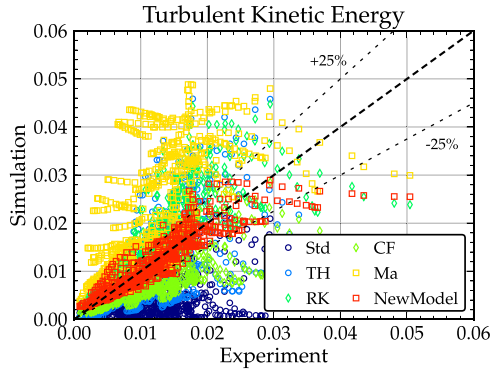


Fig. 17. Assembled BIT Model Assessment: Spread plot comparing predicted k profiles (y-axis) with experimental values (x-axis) for entire Liu (1989) database. All 42 sets are considered for radial values in the bulk ($r/R < 0.8$).

delivers considerably improved turbulent kinetic energy predictions that are in close agreement with the experimental measurements.

5.2. Error spreads

BIT model performance for the entire Liu (1989) experimental database is visualized through aid of a spread plot, where the turbulent kinetic energy predictions (y-axis) are plotted against their corresponding experimental values (x-axis). All 42 sets are considered for radial values in the bulk ($r/R < 0.8$). The thick dashed line denotes perfect agreement and the dotted lines signify 25% error bounds. As demonstrated in Fig. 17, the majority of Std, TH, and CF predictions reside below the thick dashed line, while the RK and Ma predictions are situated above. The NewModel performs considerably better than all tested formulations, delivering k predictions that straddle the center-line.

5.3. Error analysis

The error distribution between turbulent kinetic energy predictions and corresponding experimental values are visualized in Fig. 18 through the use of box plots and empirical cumulative distribution function (CDF) plots. All 42 sets are again considered for radial values in the bulk ($r/R < 0.8$). Regarding the box plot (Fig. 18a), the box itself characterizes the inner quartile range (IQR) of the error distribution; the center-line inside the box indicates the median value; and the whiskers at the periphery connected to the box by dashes represent the lowest/highest datum still within

1.5 IQR of the lower/upper quartiles. The Std, TH, and CF models significantly underpredict k , whereas RK and Ma overpredict it. The NewModel exhibits improved prediction performance, evidenced by a median error near 0% and the smallest IQR. The empirical CDF (Fig. 18b) conveys this same information in a different manner, revealing the fraction of total error that lies within a given percentile. The resulting plot further exemplifies the performance of the newly assembled model, with 80% of k predictions residing within 25% error.

6. Conclusion

A bubble-induced turbulence (BIT) model has been assembled that incorporates additional physical understanding into its formulation by leveraging DNS analyses, experimental campaigns, and prior assessment of existing closures. The assembled model comprises five components that include: a new turbulent viscosity (ν_t) formulation derived from the two-phase quasi-equilibrium turbulent kinetic energy balance; a new time-scale (τ) formulation based on bubble characteristics informed by energy spectra and two-point correlation analyses; and optimized formulations for the modulation parameter (K_{BI}), dissipation coefficient ($C_{\varepsilon B}$), and newly proposed turbulent viscosity multiplier ($C_{\mu B}$) obtained through simulation of specific turbulent regimes inherent to the Liu (1989) experimental database.

Model performance is examined through simulation of the entire Liu (1989) experimental database and direct comparison with the Standard (no BIT), Troshko and Hassan (2001), Rzehak and Krepper (2013), Colombo and Fairweather (2015), and Ma et al. (2017) closures. Both qualitative inspection of individual sets as well as quantitative assessment of the error distribution demonstrate the assembled model's considerable improvement in turbulent kinetic energy prediction, wherein 80% of such predictions reside within 25% of cumulative error.

6.1. Model strengths and limitations

The primary strength of the model derives from the decoupling strategy applied during its construction to ensure physically consistent volume fraction and relative velocity distributions (see Section 2.1.1). This methodology embeds the proper physics into the model formulation (rather than tuning for a particular set of momentum closures), and consequently, as existing momentum closures are improved, the turbulence predictions delivered from the assembled model should also improve consistently. Further, model performance and applicability has been extended by linking key parameters (i.e., K_{BI} , $C_{\varepsilon B}$, and $C_{\mu B}$) with specific turbulent regimes during optimization.

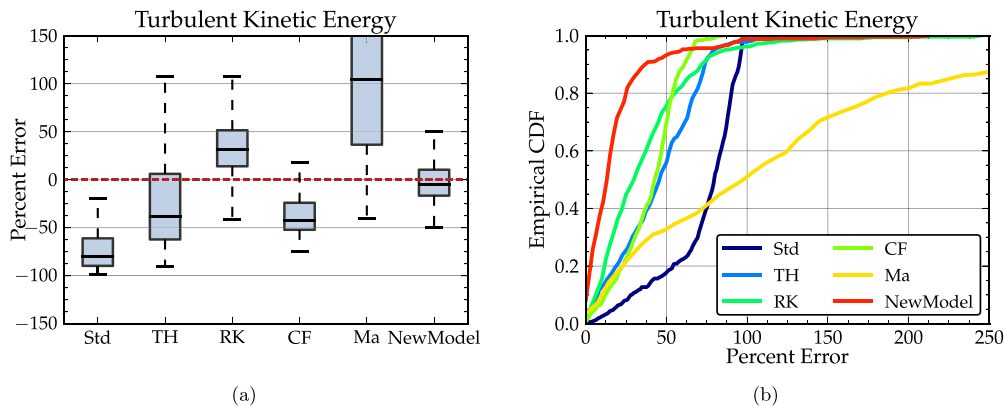


Fig. 18. Assembled BIT Model Assessment: Error distribution of k prediction for entire Liu (1989) database visualized using (a) box and (b) empirical CDF plots. All 42 sets are considered for radial values in the bulk ($r/R < 0.8$).

The primary limitation of the model is the scarce number of databases that could be leveraged during its formulation. Important two-phase turbulent mechanisms have been inferred from a small set of DNS cases, which have been optimized via the only available experimental database that reports sufficient mean (α_G , U_L , U_G , and D_B) and turbulent (u , v , w , and uv) distributions.

6.2. Model implementation

Since the model is assembled using decoupled interfacial forces, a brief discussion regarding its implementation and re-coupling with momentum closure relations is worthwhile. While the Tomiyama et al. (1998) drag and constant lift coefficient formulations are largely insensitive to the BIT model, the Burns et al. (2004) turbulent dispersion and Lubchenko et al. (2018) wall lubrication forces are not as they both depend on the turbulent viscosity (μ_{tL}). The assembled model predicts a higher turbulent viscosity profile, and consequently, the resulting turbulent dispersion force becomes over-powered and serves to flatten/smear the radial void fraction distribution. This effect can be mitigated by increasing the turbulent dispersion coefficient (σ_{TD}), as discussed in Appendix A. Immediate future work involves model re-coupling, calibration, and integration with the Bubbly And Moderate void Fraction (BAMF) formulation (Sugrue et al., 2017) through the development of a functional relation for this parameter.

6.3. Recommended future work

Future improvements should seek to develop functional formulations for the modulation parameter (K_{BI}), dissipation coefficient ($C_{\varepsilon B}$), and turbulent viscosity multiplier ($C_{\mu B}$) terms. Doing so requires complementary research efforts with respect to momentum closure development, new experimental campaigns, and DNS parametric studies.

Overall performance can be enhanced through improvements to momentum closure relations. Since the drag force and relative velocity between phases manifest in the source term formulations, improvements to drag will directly benefit model performance. Likewise, better understanding and quantification of the lateral redistribution forces (namely, lift and turbulent dispersion) will improve prediction of the radial volume fraction distribution, which directly manifests in the BIT source terms.

New experimental campaigns that record sufficient mean and turbulent quantities are absolutely necessary. The primary limitation of the assembled model is related to the limited number of databases that could be leveraged during its formulation. Additional experimental databases will help improve physical understanding by providing large volumes of data to support model development, optimization, and assessment.

DNS parametric studies are essential for improving physical understanding of the complex bubble-induced turbulence mechanisms.

Future studies, at a minimum, must compute mean and turbulent distributions, turbulent kinetic energy budgets, and two-point correlations for the entire wall-normal direction. Additionally, the turbulent viscosity should be computed to examine its two-phase profile and the validity of the eddy-viscosity assumption. Further, these quantities should be computed as part of a parametric study to systematically probe the effects of important fluid properties that include volume fraction (α_G), friction Reynolds number (Re_τ), bubble diameter (D_B), and bubble deformability. Armed with such a test matrix and computed turbulent quantities, it will be possible to identify key mechanisms, improve formulations, and calibrate the constituent BIT closure components. For example, the bubble diameter and local volume fraction can be used to calibrate the time-scale (τ); likewise, bubble deformability could be linked to the modulation parameter (K_{BI}) and dissipation coefficient ($C_{\varepsilon B}$).

Acknowledgments

This research was partially supported by the Consortium for Advanced Simulation of Light Water Reactors (<http://www.casl.gov>), an Energy Innovation Hub (<http://www.energy.gov/hubs>) for Modeling and Simulation of Nuclear Reactors under U.S. Department of Energy Contract No. DE-AC05-00OR22725. This research was also performed under appointment to the Rickover Fellowship Program in Nuclear Engineering sponsored by the Naval Reactors Division of the U.S. Department of Energy.

Appendix A. Model Implementation

The new BIT model is assembled by decoupling the non-linear feedback relationship between interfacial forces and turbulence (see Section 2.1.1). This achieves physically consistent volume fraction and relative velocity distributions during model construction, which ensures that model parameters are optimized according to the correct physics. However, when re-coupling the turbulence and momentum closure relations, the Burns et al. (2004) turbulent dispersion and Lubchenko et al. (2018) wall lubrication forces require recalibration to accommodate the increased turbulent viscosity (μ_{tL}) predictions delivered by the BIT model; otherwise, the resulting turbulent dispersion force becomes over-powered and serves to flatten/smear the radial void fraction distribution.

A suitable approach to mitigate this behavior is to employ a turbulent dispersion coefficient (σ_{TD}) equal to 3.0. This action reduces the magnitude of the Burns et al. (2004) turbulent dispersion and Lubchenko et al. (2018) wall lubrication forces, as this term arises in the denominator of the expressions. As demonstration and validation of this approach, consider again the prediction performance of the gas volume fraction (α_G), gas velocity (U_G), liquid velocity (U_L), turbulent viscosity (ν_t), and liquid turbulent kinetic energy (k) for the fourth row of the Liu (1989) experimental database illustrated in Fig. A1.

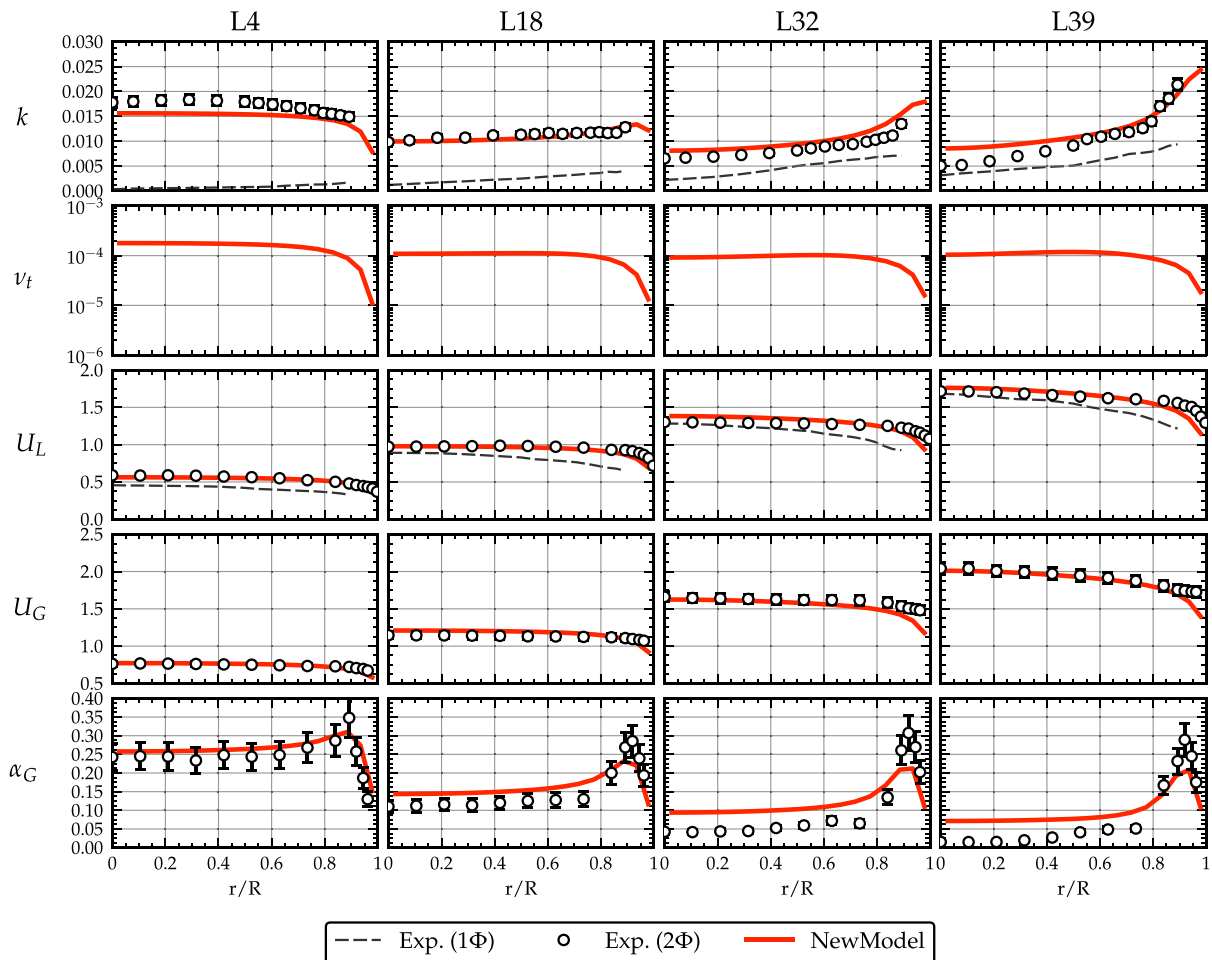


Fig. A1. Assembled Model Implementation: Using Burns et al. (2004) turbulent dispersion and Lubchenko et al. (2018) wall lubrication with $\sigma_{TD}=3.0$ delivers accurate predictions, as demonstrated for selected sets from fourth row ($j_G = 0.18$ m/s) of Liu (1989) experimental database. Traversing rightwards denotes increasing j_L (0.376, 0.753, 1.087, and 1.391 m/s).

Supplementary material

Supplementary material associated with this article can be found, in the online version, at doi:[10.1016/j.ijmultiphaseflow.2019.04.009](https://doi.org/10.1016/j.ijmultiphaseflow.2019.04.009).

References

- Batchelor, G.K., 2000. An Introduction to Fluid Dynamics. Cambridge University Press, Cambridge, UK doi:[10.1017/CBO9780511800955](https://doi.org/10.1017/CBO9780511800955).
- Bolotnov, I.A., Lahey Jr., R.T., Drew, D.A., Jansen, K.E., 2008a. Turbulent cascade modeling of single and bubbly two-phase turbulent flows. *Int. J. Multiphase Flow* 34, 1142–1151. doi:[10.1016/j.ijmultiphaseflow.2008.06.006](https://doi.org/10.1016/j.ijmultiphaseflow.2008.06.006).
- Bolotnov, I.A., Lahey Jr., R.T., Drew, D.A., Jansen, K.E., Oberai, A.A., 2008b. A spectral turbulent cascade model for single- and two-phase uniform shear flows. *J. Turbulence* 9. doi:[10.1080/14685240802261102](https://doi.org/10.1080/14685240802261102).
- Brown, C.S., Bolotnov, I.A., 2016. Spectral analysis of single- and two-phase bubbly DNS in different geometries. *Nuclear Sci Eng* 184, 363–376. doi:[10.13182/NSE15-126](https://doi.org/10.13182/NSE15-126).
- Bunner, B., Tryggvason, G., 2003. Effect of bubble deformation on the properties of bubbly flows. *J. Fluid Mech* 495, 77–118. doi:[10.1017/S0022112003006293](https://doi.org/10.1017/S0022112003006293).
- Burns, A.D., Frank, T., Hamill, I., Shi, J.-M., 2004. The Favre averaged drag model for turbulent dispersion in eulerian multi-phase flows. In: 5th International Conference on Multiphase Flow, ICMF'04, Yokohama, Japan, May 30 – June 4.
- Colombo, M., Fairweather, M., 2015. Multiphase turbulence in bubbly flows: rans simulations. *Int. J. Multiphase Flow* 77, 222–243. doi:[10.1016/j.ijmultiphaseflow.2015.09.003](https://doi.org/10.1016/j.ijmultiphaseflow.2015.09.003).
- Drew, D.A., Passman, S.L., 1999. Theory of Multicomponent Fluids. Springer-Verlag, New York, NY.
- Feng, J., Bolotnov, I.A., 2017. Evaluation of bubble-induced turbulence using direct numerical simulation. *Int. J. Multiphase Flow* 93, 92–107. doi:[10.1016/j.ijmultiphaseflow.2017.04.003](https://doi.org/10.1016/j.ijmultiphaseflow.2017.04.003).
- Hibiki, T., Ishii, M., 1999. Experimental study on interfacial area transport in bubbly two-phase flows. *Int. J. Heat Mass Transfer* 42, 3019–3035. doi:[10.1016/S0017-9310\(99\)00014-9](https://doi.org/10.1016/S0017-9310(99)00014-9).
- Hibiki, T., Ishii, M., Xiao, Z., 2001. Axial interfacial area transport of vertical bubbly flows. *Int. J. Heat Mass Transfer* 44, 1869–1888. doi:[10.1016/S0017-9310\(00\)00232-5](https://doi.org/10.1016/S0017-9310(00)00232-5).
- Hosokawa, S., Tomiyama, A., 2009. Multi-fluid simulation of turbulent bubbly pipe flows. *Chem. Eng. Sci.* 64, 5308–5318. doi:[10.1016/j.ces.2009.09.017](https://doi.org/10.1016/j.ces.2009.09.017).
- Hosokawa, S., Tomiyama, A., 2013. Bubble-induced pseudo turbulence in laminar pipe flows. *Int. J. Heat Fluid Flow* 40, 97–105. doi:[10.1016/j.ijheatfluidflow.2013.01.004](https://doi.org/10.1016/j.ijheatfluidflow.2013.01.004).
- Ishii, M., Hibiki, T., 2011. Thermo-Fluid Dynamics of Two-Phase Flow. Springer-Verlag, New York, NY.
- Jones, W., Launder, B., 1972. The prediction of laminarization with a two-equation model of turbulence. *Int. J. Heat Mass Transfer* 15, 301–314. doi:[10.1016/0017-9310\(72\)90076-2](https://doi.org/10.1016/0017-9310(72)90076-2).
- Kataoka, I., Serizawa, A., 1989. Basic equations of turbulence in gas-liquid two-phase flow. *Int. J. Multiphase Flow* 15, 843–855. doi:[10.1016/0301-9322\(89\)90045-1](https://doi.org/10.1016/0301-9322(89)90045-1).
- Kataoka, I., Serizawa, A., Besnard, D.C., 1993. Prediction of turbulence suppression and turbulence modeling in bubbly two-phase flow. *Nuclear Eng. Des.* 141, 145–158. doi:[10.1016/0029-5493\(93\)90099-U](https://doi.org/10.1016/0029-5493(93)90099-U).
- Lahey, R.T., 2005. The simulation of multidimensional multiphase flows. *Nuclear Eng. Des.* 235, 1043–1060. Festschrift Edition Celebrating the 65th Birthday of Prof. Richard T. Lahey, Jr. doi:[10.1016/j.nucengdes.2005.02.020](https://doi.org/10.1016/j.nucengdes.2005.02.020).
- Lance, M., Bataille, J., 1991. Turbulence in the liquid phase of a uniform bubbly air-water flow. *J. Fluid Mech* 222, 95–118. doi:[10.1017/S0022112091001015](https://doi.org/10.1017/S0022112091001015).
- Launder, B., Sharma, B., 1974. Application of the energy-dissipation model of turbulence to the calculation of flow near a spinning disc. *Lett. Heat Mass Transfer* 1, 131–137. doi:[10.1016/0094-4548\(74\)90150-7](https://doi.org/10.1016/0094-4548(74)90150-7).
- Launder, B., Spalding, D., 1974. The numerical computation of turbulent flows. *Comput. Method. Appl. Mech.Eng.* 3, 269–289.
- Leal, L.G., 1989. Vorticity transport and wake structure for bluff bodies at finite Reynolds number. *Phys. Fluids* 1, 124–131. doi:[10.1063/1.857540](https://doi.org/10.1063/1.857540).

- Lee, S., Lahey Jr., R.T., Jones, O.C., 1989. The prediction of two-phase turbulence and phase distribution using a $k-\epsilon$ model. *Japanese J. Multiphase Flow* 3, 335–368. doi:[10.1115/1.2910220](#).
- Lelouvetel, J., Tanaka, T., Sato, Y., Hishida, K., 2014. Transport mechanisms of the turbulent energy cascade in upward/downward bubbly flows. *J. Fluid Mech.* 741, 514–542. doi:[10.1017/jfm.2014.24](#).
- Liu, T.J., 1989. *Experimental Investigation of Turbulence Structure in Two-Phase Bubbly Flow*. Northwestern University, Evanston, Illinois Ph.D. thesis.
- Liu, T.J., Bankoff, S.G., 1993a. Structure of air-water bubbly flow in a vertical pipe-i. liquid mean velocity and turbulence measurements. *Int. J. Heat Mass Transfer* 36, 1049–1060. doi:[10.1016/S0017-9310\(05\)80289-3](#).
- Liu, T.J., Bankoff, S.G., 1993b. Structure of air-water bubbly flow in a vertical pipe-ii. void fraction, bubble velocity and bubble size distribution. *Int. J. Heat Mass Transfer* 36, 1061–1072. doi:[10.1016/S0017-9310\(05\)80290-X](#).
- Lopez de Bertodano, M., Lahey Jr., R.T., Jones, O.C., 1994. Development of a $k-\epsilon$ model for bubbly two-phase flow. *J. Fluids Eng.* 116, 128–134. doi:[10.1115/1.2910220](#).
- Lopez de Bertodano, M., Lee, S.J., Lahey Jr., R.T., Drew, D.A., 1990. The prediction of two-phase turbulence and phase distribution phenomena using a reynolds stress model. *J. Fluids Eng.* 112, 107–113. doi:[10.1115/1.2909357](#).
- Lu, J., Tryggvason, G., 2008. Effect of bubble deformability in turbulent bubbly up-flow in a vertical channel. *Phys. Fluids* 20. doi:[10.1063/1.2911034](#).
- Lubchenko, N., Magolan, B., Sugrue, R., Baglietto, E., 2018. A more fundamental wall lubrication force from turbulent dispersion regularization for multiphase cfd applications. *Int. J. Multiphase Flow* 98, 36–44. doi:[10.1016/j.ijmultiphaseflow.2017.09.003](#).
- Ma, T., Santarelli, C., Ziegenhein, T., Lucas, D., Fröhlich, J., 2017. Direct numerical simulation-based reynolds-averaged closure for bubble-induced turbulence. *Phys. Rev. Fluids* 2, 034301. doi:[10.1103/PhysRevFluids.2.034301](#).
- Magolan, B., Baglietto, E., Brown, C., Bolotnov, I.A., Tryggvason, G., Lu, J., 2017. Multiphase turbulence mechanisms identification from consistent analysis of direct numerical simulation data. *Nuclear Eng. Technol.* 49, 1318–1325. doi:[10.1016/j.net.2017.08.001](#).
- Magolan, B., Lubchenko, N., Baglietto, E., 2019. A quantitative and generalized assessment of bubble-induced turbulence models for gas-liquid systems. *Chem. Eng. Sci.* X 2, 100009. doi:[10.1016/j.cesx.2019.100009](#).
- Martínez Mercado, J., Chehata Gómez, D., Van Gils, D., Sun, C., Lohse, D., 2010. On bubble clustering and energy spectra in pseudo-turbulence. *J. Fluid Mech.* 650, 287–306. doi:[10.1017/S0022112009993570](#).
- Mendez-Díaz, S., Serrano-García, J.C., Zenit, R., Hernández-Cordero, J.A., 2013. Power spectral distributions of pseudo-turbulent bubbly flows. *Phys. Fluids* 25. doi:[10.1063/1.4800782](#).
- Michiyoshi, I., Serizawa, A., 1986. Turbulence in two-phase bubbly flow. *Nuclear Eng. Des.* 95, 253–267. doi:[10.1016/0029-5493\(86\)90052-X](#).
- Morel, C., 1997. *Turbulence modeling and first numerical simulation in turbulent two-phase flows*. Technical Report. CEA Grenoble, France.
- Nakoryakov, V.E., Kashinsky, O.N., Randin, V.V., Timkin, L.S., 1996. Gas-liquid bubbly flow in vertical pipes. *J. Fluids Eng.* 118, 377–382. doi:[10.1115/1.2817389](#).
- Panidis, T., 2011. The development of the structure of water-air bubble grid turbulence. *Int. J. Multiphase Flow* 37, 565–575. doi:[10.1016/j.ijmultiphaseflow.2011.03.010](#).
- Panidis, T., Papailiou, D.D., 2000. The structure of two-phase grid turbulence in a rectangular channel: an experimental study. *Int. J. Multiphase Flow* 26, 1369–1400. doi:[10.1016/S0301-9322\(99\)00085-3](#).
- Politano, M., Carrica, P., Conventi, J., 2003. A model for turbulent polydisperse two-phase flow in vertical channels. *Int. J. Multiphase Flow* 29, 1153–1182. doi:[10.1016/S0301-9322\(03\)00065-X](#).
- Prakash, V.N., Martínez Mercado, J., van Wijngaarden, L., Mancilla, E., Tagawa, Y., Lohse, D., Sun, C., 2016. Energy spectra in turbulent bubbly flows. *J. Fluid Mech.* 791, 174–190. doi:[10.1017/jfm.2016.49](#).
- Riboux, G., Legendre, D., Risso, F., 2013. A model of bubble-induced turbulence based on large-scale wake interactions. *J. Fluid Mech.* 719, 362–387. doi:[10.1017/jfm.2013.12](#).
- Riboux, G., Risso, F., Legendre, D., 2010. Experimental characterization of the agitation generated by bubbles rising at high Reynolds number. *J. Fluid Mech.* 643, 509–539. doi:[10.1017/S0022112009992084](#).
- Risso, F., 2011. Theoretical model for k^{-3} spectra in dispersed multiphase flows. *Phys. Fluids* 23. doi:[10.1063/1.3530438](#).
- Roghair, I., Martínez Mercado, J., Van Sint Annaland, M., Kuipers, H., Sun, C., Lohse, D., 2011. Energy spectra and bubble velocity distributions in pseudo-turbulence: numerical simulations vs. experiments. *Int. J. Multiphase Flow* 37, 1093–1098. doi:[10.1016/j.ijmultiphaseflow.2011.07.004](#).
- Rzehak, R., Krepper, E., 2013. Cfd modeling of bubble-induced turbulence. *Int. J. Multiphase Flow* 55, 138–155. doi:[10.1016/j.ijmultiphaseflow.2013.04.007](#).
- Santarelli, C., Fröhlich, J., 2015. Direct numerical simulations of spherical bubbles in vertical turbulent channel flow. *Int. J. Multiphase Flow* 75, 174–193. doi:[10.1016/j.ijmultiphaseflow.2015.05.007](#).
- Santarelli, C., Fröhlich, J., 2016. Direct numerical simulations of spherical bubbles in vertical turbulent channel flow. influence of bubble size and bidispersity. *Int. J. Multiphase Flow* 81, 27–45. doi:[10.1016/j.ijmultiphaseflow.2016.01.004](#).
- Santarelli, C., Roussel, J., Fröhlich, J., 2016. Budget analysis of the turbulent kinetic energy for bubbly flow in a vertical channel. *Chem. Eng. Sci.* 141, 46–62. doi:[10.1016/j.ces.2015.10.013](#).
- Sato, Y., Sadatomi, M., Sekoguchi, K., 1981. Momentum and heat transfer in two-phase bubble flow-i. theory. *Int. J. Multiphase Flow* 7, 167–177. doi:[10.1016/0301-9322\(81\)90003-3](#).
- Sato, Y., Sekoguchi, K., 1975. Liquid velocity distribution in two-phase bubble flow. *Int. J. Multiphase Flow* 2, 79–95. doi:[10.1016/0301-9322\(75\)90030-0](#).
- Serizawa, A., Kataoka, I., Michiyoshi, I., 1975. Turbulence structure of air-water bubbly flow-ii. local properties. *Int. J. Multiphase Flow* 2, 235–246. doi:[10.1016/0301-9322\(75\)90012-9](#).
- Shaver, D., Podowski, M., 2015. *Modeling of interfacial forces for bubbly flows in subcooled boiling conditions*. In: *Transactions of the American Nuclear Society*, pp. 1368–1371.
- Shawkat, M.E., Ching, C.Y., 2011. Liquid turbulence kinetic energy budget of co-current bubbly flow in a large diameter vertical pipe. *J. Fluids Eng.* 133. doi:[10.1115/1.4003855](#).
- Shawkat, M.E., Ching, C.Y., Shoukri, M., 2007. On the liquid turbulence energy spectra in two-phase bubbly flow in a large diameter vertical pipe. *Int. J. Multiphase Flow* 33, 300–316. doi:[10.1016/j.ijmultiphaseflow.2006.09.002](#).
- Shawkat, M.E., Ching, C.Y., Shoukri, M., 2008. Bubble and liquid turbulence characteristics of bubbly flow in a large diameter vertical pipe. *Int. J. Multiphase Flow* 34, 767–785. doi:[10.1016/j.ijmultiphaseflow.2008.01.007](#).
- Sugrue, R., Magolan, B., Lubchenko, N., Baglietto, E., 2017. Assessment of a simplified set of momentum closure relations for low volume fraction regimes in star-ccm+ and openfoam. *Annals of Nuclear Energy* 110, 79–87. doi:[10.1016/j.anucene.2017.05.059](#).
- Tomiyama, A., Kataoka, I., Zun, I., Sakaguchi, T., 1998. Drag coefficients of single bubbles under normal and micro gravity conditions. *JSME Int. J. Ser. B* 41, 472–479. doi:[10.1299/jsmeb.41.472](#).
- Troshko, A., Hassan, Y., 2001. A two-equation turbulence model of turbulent bubbly flows. *Int. J. Multiphase Flow* 27, 1965–2000. doi:[10.1016/S0301-9322\(01\)00043-X](#).
- Vaidheeswaran, A., Hibiki, T., 2017. Bubble-induced turbulence modeling for vertical bubbly flows. *Int. J. Heat Mass Transfer* 115, 741–752. doi:[10.1016/j.ijheatmasstransfer.2017.08.075](#).
- Wang, S.K., 1985. *Three-dimensional turbulence measurements in air/water two-phase flow*. Rensselaer Polytechnic Institute, Troy, New York Ph.D. thesis.
- Wang, S.K., Lee, S.J., Jones, O.C., Lahey Jr., R.T., 1987. 3-D turbulence structure and phase distribution measurements in bubbly two-phase flows. *Int. J. Multiphase Flow* 13, 327–343. doi:[10.1016/0301-9322\(87\)90052-8](#).
- Wang, S.K., Lee, S.J., Jones, O.C., Lahey Jr., R.T., 1990. Statistical analysis of turbulent two-phase pipe flow. *J. Fluids Eng.* 112, 89–95. doi:[10.1115/1.2909374](#).
- Weller, H.G., Tabor, G., Jasak, H., Fureby, C., 1998. A tensorial approach to computational continuum mechanics using object-oriented techniques. *Comput. Phys.* 12, 620–631. doi:[10.1063/1.168744](#).
- Yeoh, G.H., Tu, J., 2010. *Computational Techniques for Multi-Phase Flows*. Butterworth-Heinemann, Oxford, UK.